



OPEN ACCESS

EDITED BY

Vasif Nejat Hasirci,
Acibadem University, Turkey

REVIEWED BY

Hee-Gyeong Yi,
Chonnam National University,
South Korea
Pinar Yilgor Huri,
Ankara University, Turkey

*CORRESPONDENCE

Marta Tunesi,
✉ marta.tunesi@polimi.it

SPECIALTY SECTION

This article was submitted to Tissue Engineering and Regenerative Medicine, a section of the journal Frontiers in Bioengineering and Biotechnology

RECEIVED 31 August 2022

ACCEPTED 06 December 2022

PUBLISHED 22 December 2022

CITATION

Merli M, Sardelli L, Baranzini N, Grimaldi A, Jacchetti E, Raimondi MT, Briatico-Vangosa F, Petrini P and Tunesi M (2022), Pectin-based bioinks for 3D models of neural tissue produced by a pH-controlled kinetics. *Front. Bioeng. Biotechnol.* 10:1032542. doi: 10.3389/fbioe.2022.1032542

COPYRIGHT

© 2022 Merli, Sardelli, Baranzini, Grimaldi, Jacchetti, Raimondi, Briatico-Vangosa, Petrini and Tunesi. This is an open-access article distributed under the terms of the [Creative Commons Attribution License \(CC BY\)](https://creativecommons.org/licenses/by/4.0/). The use, distribution or reproduction in other forums is permitted, provided the original author(s) and the copyright owner(s) are credited and that the original publication in this journal is cited, in accordance with accepted academic practice. No use, distribution or reproduction is permitted which does not comply with these terms.

Pectin-based bioinks for 3D models of neural tissue produced by a pH-controlled kinetics

Marta Merli¹, Lorenzo Sardelli¹, Nicolò Baranzini², Annalisa Grimaldi², Emanuela Jacchetti¹, Manuela Teresa Raimondi¹, Francesco Briatico-Vangosa¹, Paola Petrini¹ and Marta Tunesi^{1*}

¹Department of Chemistry, Materials and Chemical Engineering "G. Natta", Politecnico di Milano, Milan, Italy, ²Department of Biotechnology and Life Sciences, University of Insubria, Varese, Italy

Introduction: In the view of 3D-bioprinting with cell models representative of neural cells, we produced inks to mimic the basic viscoelastic properties of brain tissue. Moving from the concept that rheology provides useful information to predict ink printability, this study improves and expands the potential of the previously published 3D-reactive printing approach by introducing pH as a key parameter to be controlled, together with printing time.

Methods: The viscoelastic properties, printability, and microstructure of pectin gels crosslinked with CaCO₃ were investigated and their composition was optimized (i.e., by including cell culture medium, HEPES buffer, and collagen). Different cell models representative of the major brain cell populations (i.e., neurons, astrocytes, microglial cells, and oligodendrocytes) were considered.

Results and Discussion: The outcomes of this study propose a highly controllable method to optimize the printability of internally crosslinked polysaccharides, without the need for additives or post-printing treatments. By introducing pH as a further parameter to be controlled, it is possible to have multiple (pH-dependent) crosslinking kinetics, without varying hydrogel composition. In addition, the results indicate that not only cells survive and proliferate following 3D-bioprinting, but they can also interact and reorganize hydrogel microstructure. Taken together, the results suggest that pectin-based hydrogels could be successfully applied for neural cell culture.

KEYWORDS

3D-printing, reactive printing, 3D-bioprinting, internal gelation, rheology, printability optimization, collagen, cell viability

1 Introduction

Rendering selected aspects of the *in vivo* complexity in a representative laboratory model can greatly enhance our understanding of physiological and pathological phenomena and provide critical and cost-effective tools for diagnostic or high throughput screening, drug discovery and the development of medical devices (Peneda Pacheco et al., 2021). However, this is particularly challenging when modelling nervous tissue. The variety and plurality of topographical and biochemical stimuli driving its development and functions have fascinated the scientific community (Papadimitriou et al., 2020). However, this poses several questions on how it is possible to model nervous tissue.

In the route to the setting up of reliable and accurate *in vitro* engineered models of neural tissue, hydrogel-based 3D models have produced concrete advancements towards this end (Antill-O'Brien et al., 2019). Indeed, although 2D models are inexpensive and highly reproducible, they lack sufficient complexity to gain insight into the biological phenomena driving brain functionality (Hopkins et al., 2015). In contrast, hydrogels provide a rudimentary 3D extra-cellular matrix to reproduce more physiological-like conditions. Both natural (e.g. alginate, chitosan, collagen) and synthetic (e.g. polyethylene glycol, polycaprolactone) polymers have been exploited (Oliveira et al., 2019), eventually coupled with glial scar-inhibiting (Lee et al., 2010) or neurotrophic factors (Taylor et al., 2006). More recently, brain decellularized extracellular matrix was also proposed to match the physical (e.g. stiffness) and biochemical properties of native tissue, and modulate biological functions (Bae et al., 2021; Zhang et al., 2021). As an alternative, blending is a common approach to design composite materials with improved properties (Zhao et al., 2020), with one polymer providing suitable mechanical features, while the other(s) promoting cell adhesion and viability.

However, a third dimension is not enough to model highly hierarchical tissues such as the brain. Proper control of the architecture, pore interconnectivity and viscoelastic properties of hydrogels, as well as the distribution of different cell populations in the 3D environment, is still an open challenge to increase the reliability of *in vitro* models of the brain (Samanipour et al., 2022). For the fabrication of highly reproducible layered-based multicellular architectures with positional control over biomaterials and cells (Qiu et al., 2020), 3D-bioprinting technologies have emerged. As the products can be shaped on the architecture of a defect, bioprinting holds a great potential for localized pathological conditions, like stroke or traumatic brain injury. Especially in a delicate environment, such as the central nervous system, direct printing on the patient could improve the integration of engineered tissue with surrounding tissue (Mehrotra et al., 2019), pushing forwards personalized healthcare (Vaz and Kumar, 2021).

Due to the similarity with the sugar-based macromolecules in the extracellular matrix of native tissues, polysaccharide-based inks are extremely common in 3D-bioprinting. Engineering their formulation and properties is fundamental to promote cell viability and easily pattern the constructs (Paxton et al., 2017). To reach the first goal, several polysaccharides require grafting with peptides such as arginine-glycine-aspartic acid (RGD) or tyrosine-isoleucine-glycine-serine-arginine (YIGSR) moieties; for the second goal, the control of crosslinking offers the possibility to tailor and shape the constructs. For example, Schwann cells were loaded in a peptide-conjugated alginate solution then crosslinked by ionotropic external gelation with calcium ions produced by the dissolution of CaCl_2 , and the system sustained cell viability (Sarker et al., 2019). As previously reported, RGD-functionalization of gellan gum proved to be effective to bioprint cortical neurons in layered structures (Lozano et al., 2015). In this case, the bioink/cell suspension and the crosslinker (e.g. CaCl_2 or 5 \times Dulbecco's modified Eagle's medium, DMEM) were loaded into different syringes and flowed through silicone tubing before automatic mixing and extrusion. According to the hypothesis that weakly crosslinked bioinks before printing can shield from potential damage to cell membranes, Lindsay et al. (2019) also pursued this strategy, but they added a post-printing crosslinking step to stabilize the constructs. They printed neural progenitor cells into RGD-functionalized alginate that had been pre-crosslinked with CaSO_4 , and then covered the samples with culture medium supplemented with CaCl_2 for a further crosslinking step. Overall, these crosslinking approaches rely on the diffusion of highly soluble calcium ions and produce inhomogeneous hydrogels (Skjåk-Bræk et al., 1989; Secchi et al., 2014). Indeed, polymer concentration decreases from the interface with the crosslinking solution to the center of the gels (Secchi et al., 2014), with impact on both cell distribution along the fiber sections and gas/nutrient diffusion.

Alginate is the most widely applied polysaccharide for cell delivery. However, it has limited chemical stability in culture media, where calcium chelators (e.g. phosphate, lactate, citrate) and monovalent cations (e.g. sodium and magnesium) may displace calcium ions. In contrast, Ca-pectinate gels are less sensitive to chemical agents and represent a better choice for cell embedding (Wan-Ping et al., 2011). Pectin, which is a versatile class of anionic and branched polysaccharides found in the cell walls of land-based plants, is regarded as the most structurally and functionally complex polysaccharide in nature (Liang and Luo, 2020). Due to its relatively low cost, stability, and gelation properties, pectin is traditionally used in food industry (Vancauwenbergh et al., 2018). Its bioavailability and biological features have also favored its use in the pharmaceutical industry (e.g. drug administration, Lara-Espinoza et al., 2018; films with antimicrobial properties, Kumar et al., 2020; wound dressing, Andriotis et al., 2020) and in tissue engineering/regenerative medicine (Munarin et al., 2011; Pereira et al., 2018; Campiglio et al., 2021).

Although pectin exhibits several bioactive properties that could be favorably applied in neural tissue engineering, its exploitation in this field is lacking. It displays metal-binding

ability (Lessa et al., 2020), cancer inhibition due to the close interaction with galectin-3 (Gao et al., 2013), and mucoadhesiveness (Sriamornsak et al., 2010). Heavy metals are involved in the control of oxidative stress (Giacoppo et al., 2014; Giampietro et al., 2018), a mechanism that leads to neurodegeneration (Bedini et al., 2021). Galectin-3 is expressed by reactive microglia. It has emerged as a potential biomarker for Alzheimer's and Parkinson's diseases, but it also promotes inflammation in traumatic brain injury (García-Revilla et al., 2022). Finally, mucoadhesiveness could be exploited for the intranasal delivery of cells to the brain (Danielyan et al., 2009). Furthermore, pectin exhibits conductive properties (Dennis et al., 2022) that could represent an effective starting point for enhancing neuronal cell adhesion and neurite formation (Zhong and Bellamkonda, 2008), although its exploitation for neural cell culture is still lacking.

Like gellan gum and alginate, low methoxyl pectin shows cation-binding capacity. It interacts with divalent cations *via* its non-methyl-esterified galacturonic acid units (Celus et al., 2018) to form ionic-bound gels stabilized by non-covalent crosslinks (external gelation). However, another mechanism is possible (i.e. internal gelation). It relies on the slow, progressive dissolution of poorly soluble calcium salts, such as CaCO₃ or calcium phosphate particles (Munarin et al., 2014), which are homogeneously mixed with pectin solution. The distinctive features of internal gelation are the time-dependent variation of viscoelastic properties as well as the production of homogeneous networks, which are more advantageous for cell culture. A key factor to drive the crosslinking kinetics is pH (Burey et al., 2008; Moreira et al., 2014), because acidic pH drives the dissolution of calcium salts. Nevertheless, as with external gelation, also in the case of internal crosslinking, polysaccharides are described to be combined with other polymer components or subjected to post-printing treatments such as crosslinking by UV light to achieve suitable viscoelastic properties and stability (Li et al., 2020; Kim et al., 2021).

In this study, we propose a highly controllable method to optimize the printability of internally crosslinked polysaccharides, without the need for additives or post-printing treatments. Starting from the concept that rheology provides useful information to predict ink printability, we expanded the 3D-reactive printing approach (Sardelli et al., 2021) by introducing pH as a key parameter to be controlled, together with printing time. We investigated the suitability of the proposed inks for 3D-printing *a priori*, by analyzing the viscoelastic properties of pectin gels crosslinked with CaCO₃. Ink composition was optimized in the view of applications with or without cell models representative of the major brain cell populations, for example by including cell culture medium and collagen. Then, 3D-bioprinted cell-laden constructs were produced according to the optimized printing conditions. Finally, the possibility of exploiting the selected ink for 3D-

printed brain models was studied by evaluating cell viability over time.

2 Materials and methods

2.1 Materials

Low methoxyl pectin from citrus fruits (classic CU 701, batch 01907714) was kindly gifted by Herbstreith & Fox (Neuenbürg, Germany) and stored at -20°C . Sodium bicarbonate was purchased from Zeta Farmaceutici (Sandrigo, Italy), calcium carbonate (CaCO₃, code 2117, batch 180,575) from Caesar & Loretz GmbH (Hilden, Germany) and 0.9% w/v sodium chloride (NaCl) from Eurospital (Trieste, Italy). N-2-hydroxyethylpiperazine-N'-2-ethanesulfonic acid (HEPES) solution (pH 7.0–7.6), collagen solution from bovine skin (3 mg/ml, batch SLCH0781), phosphate buffered saline (PBS), resazurin sodium salt, sodium citrate tribasic, sodium hydroxide and reagents for microstructural characterization were obtained from Sigma-Aldrich (Merck KGaA, Darmstadt, Germany). Plasticware was purchased from Corning (Corning, NY, United States), while 3-(4,5-dimethylthiazol-2-yl)-5-(3-carboxymethoxyphenyl)-2-(4-sulfophenyl)-2H-tetrazolium (MTS) was Promega (Madison, WI, United States). Reagents for cell culture and confocal microscopy were obtained from Thermo Fisher Scientific (Waltham, MA, United States).

2.2 Experimental procedures

2.2.1 Material preparation

For the sake of clarity, inks were labelled as $P_xCayColl-Z$, where x represents pectin concentration (% w/v), y is CaCO₃ concentration (mmol), Coll highlights the possible presence of collagen, and Z is the solvent for pectin solutions and CaCO₃ suspensions (Table 1). For P_{2.4}Ca₂₀-NaCl and P_{2.4}Ca₃₅-NaCl, 2.4% w/v pectin was dissolved overnight in 0.9% w/v NaCl. To partially neutralize the carboxyl groups of pectin backbone, while preventing β -elimination, 20 mM NaHCO₃ was progressively added. pH was adjusted to 3.4 ± 0.1 (pHmeter Edge[®], Hanna Instruments, Woonsocket, RI, United States) with 0.75 M NaHCO₃. To promote hydrogel formation, CaCO₃ suspensions (20 or 35 mM) were prepared in 0.9% w/v NaCl and mixed with pectin (1:1.5, volumetric ratio).

For P_{3.8}Ca₂₀-DMEM and P₄Ca₂₀-DMEM, pectin (3.8% or 4% w/v, respectively) was dissolved in high glucose DMEM (code 10938-025) supplemented with 10% v/v fetal bovine serum (FBS), 2 mM L-glutamine, 100 U/ml penicillin and 100 $\mu\text{g}/\text{ml}$ streptomycin sulfate. pH was adjusted to 3.5 ± 0.1 . CaCO₃ suspensions (20 mM) were prepared in the same medium and mixed with pectin (1:1.5, volumetric ratio).

TABLE 1 Hydrogel labeling. Hydrogels were labelled as $P_xCayColl-Z$, where x represents pectin concentration, y is $CaCO_3$ concentration, $Coll$ highlights the possible presence of collagen, and Z is the solvent for pectin solutions and $CaCO_3$ suspensions.

Hydrogels ($P_xCayColl-Z$)	x , pectin (% w/v)	y , $CaCO_3$ (mmol)	$Coll$, COLLAGEN	Z , medium for pectin and $CaCO_3$
$P_{2.4}Ca_{20}$ -NaCl	2.4	20	Not present	0.9% w/v NaCl
$P_{2.4}Ca_{35}$ -NaCl		35		
P_4Ca_{20} -DMEM	4	20		DMEM
$P_{3.8}Ca_{20}$ -DMEM	3.8		Present	DMEM supplemented with HEPES
$P_{3.8}Ca_{20}Coll$ -DMEM HEPES				

For $P_{3.8}Ca_{20}Coll$ -DMEM HEPES, 3.8% w/v pectin was dissolved in DMEM also supplemented with 10 mM HEPES. pH was adjusted to 3.65 ± 0.1 . $CaCO_3$ suspensions (20 mM) were prepared in the same medium, mixed with pectin (1:1.5, volumetric ratio) and 3 min later with collagen 2.16 mg/ml (1:0.25, volumetric ratio). Collagen solution was obtained by diluting eight parts v/v bovine collagen with one part v/v PBS 10x and one part v/v 0.1 N NaOH, and then by mixing with DMEM HEPES (9:1, volumetric ratio).

For cell experiments, pectin was disinfected by washing it for three times (15 min/each) in ethanol and drying it in a laminar flow cabinet, while $CaCO_3$ was heated overnight in an oven at 121°C.

2.2.2 Rheological characterization and pH measurements

Rheological characterization was performed with a rotational rheometer (Modular Compact Rheometer MCR 502, Anton Paar, Graz, Austria) equipped with parallel-plate geometry (diameter: 25 mm; working gap: 0.5 mm). Experiments were run at $25 \pm 0.01^\circ C$, controlling the temperature with a Peltier system.

To assess their reproducibility, before mixing with $CaCO_3$, the viscosity of pectin solutions was measured in steady state shear experiments, which were performed at shear rates increasing from 0.1 to $100 s^{-1}$. Gelation kinetics was investigated by oscillatory time sweeps at 1.0 Hz and 0.5% shear strain amplitude for 140 min from the instant ($t = 0$) in which pectin was mixed with $CaCO_3$. To ensure measurements in the linear regime, the linear viscoelastic region (LVR) was defined preliminarily to other tests by applying oscillatory shear amplitude ramps (logarithmic increase from 0.01 to 1000%, frequency 1.0 Hz) to fully gelled samples (i.e. 24 h after mixing pectin with $CaCO_3$). The limit of the LVR was defined as the maximum shear strain amplitude after which the storage (G') and loss (G'') moduli start changing from the previous constant value. During the first hour of crosslinking, pH was assessed every 5 min.

To study the time dependence of flowability and structure recovery within a time window suitable for 3D-bioprinting, samples were extruded in a Petri dish immediately after

mixing (0 min), moved to the rheometer with a spatula and tested after 0, 30, 60 min crosslinking. Flowability was deduced from the viscosity curve obtained in a steady state shear test at shear rates increasing from 0.01 to $2,000 s^{-1}$. Only data acquired from the lowest shear rate to the maximum shear rate not inducing material removal from the rheometer geometry, was considered.

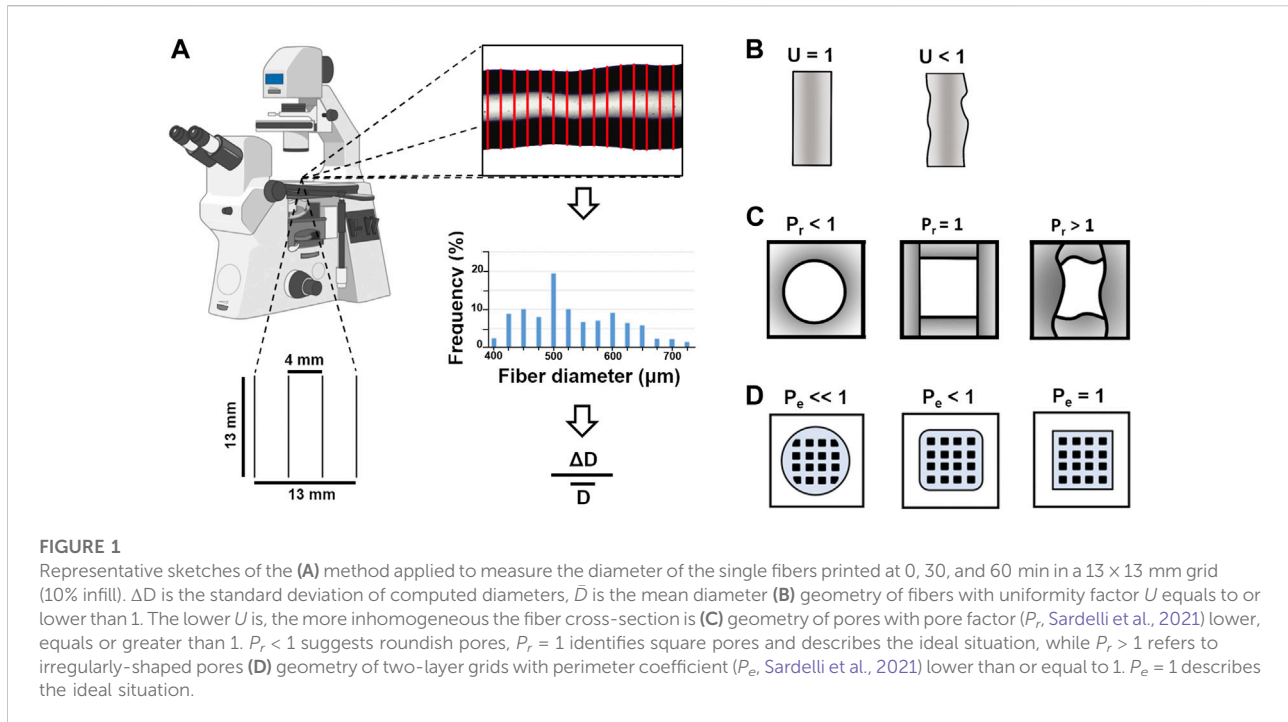
Hydrogel ability to recover their state after injection was estimated by the following three-step oscillation protocol: first, an oscillatory test was carried out for 100 s at 1.0 Hz and 0.5% strain amplitude to assess the pristine dynamic mechanical properties (G' , G''). Second, a 100% amplitude strain was applied at the same frequency for 100 s to cause a possible structural breakdown, and finally a third oscillatory step was carried out for 200 s in the same conditions as the first one to measure the recovery of G' , G'' and thus assess the material ability to recover its pristine behavior and relevant microstructure.

The stress required to extrude the material was estimated from the measurements of the yield stress after 60 min crosslinking. Oscillatory tests were run at 1.0 Hz by increasing stress amplitude from 0.1 to 100 Pa. The yield stress was defined as the value of the shear stress at which $G' = G''$ and the hydrogels undergo a transition from a solid- ($G' > G''$, $\tan\delta < 1$) to a liquid-like behavior ($G' < G''$, $\tan\delta > 1$).

2.2.3 Printability evaluation

Inks (2.5 ml in 3 ml syringes) were printed with the pneumatic-based extrusion bioprinter Inkredible⁺™ (Cellink, Gothenburg, Sweden) using conical 32 mm-length nozzles. The process applied a predefined code in Repetier-Host (Hot-World GmbH & Co. KG, Willich, Germany) operating in Slic3r (<https://slic3r.org>). Before cell loading or printing, inks were centrifuged (e.g., 800 rpm for 5 min) to remove air bubbles. Infill pattern, printing speed and layer height were varied to print fibers, two-layer geometries and five-layer grids.

Single fibers were printed after 0, 30, 60 min crosslinking (Figure 1A). Inks in 0.9% w/v NaCl were printed with 410 or 250 μm nozzles (22 or 25 G, respectively) at 10, 15, 25 mm/s; inks in DMEM w/or w/o HEPES were printed with 250 μm nozzles at 10, 15 mm/s. To study the effect of printing



pressure on fiber diameter, pressure was progressively increased by 4 kPa during the same printing, starting from the minimal pressure for a continuous flow. We defined the maximum pressure as the highest pressure at which we could print without issues, such as extruding a considerable amount of material from the cartridge or blocking the printer. Immediately after printing and before shrinkage due to solvent evaporation, fibers were imaged by an optical microscope (Eclipse Ti2, Nikon, Tokyo, Japan). To account for diameter inhomogeneity during extrusion, the initial, middle and final parts of the fibers were dimensioned. For each image, fiber diameter was measured every 10 pixels by a custom plug-in of ImageJ (<http://imagej.nih.gov/ij/>) and 290 measurements were obtained to estimate diameter distribution and mean values. Fiber uniformity was evaluated by uniformity factor (U , Figure 1B), according to Eq. 1:

$$U = 1 - \frac{\Delta D}{\bar{D}} \quad (1)$$

where ΔD is the standard deviation (SD) of computed diameters and \bar{D} is the mean diameter.

After 0, 30 min crosslinking, two-layer geometries (25 mm × 25 mm × 0.6 mm, 25% infill) were printed at 10, 15 mm/s with 250 μm nozzles. They were made up of two parallel layers superimposed perpendicularly to each other. Each layer was limited by a square border. While printing, pressure was manually adjusted to ensure uniformity and shape integrity. Constructs were imaged following printing. To assess shape

fidelity, i.e. the shape retention of the printed construct as a whole compared to the original computer design (Gillispie et al., 2020), pore factor (P_r , Figure 1C) and perimeter coefficient (P_e , Figure 1D) were calculated according to Eqs. 2 and 3 (Sardelli et al., 2021):

$$P_r = \frac{(\text{Pore Perimeter})^2}{16 \cdot (\text{Pore Area})} \quad (2)$$

$$P_e = \frac{1}{\left\{ \left[\frac{1}{2} \cdot \left(\frac{\bar{L}_x}{L_x} \cdot \frac{\bar{L}_y}{L_y} \right) - 1 \right] + 1 \right\} \cdot \left[1 + \frac{1}{2} \cdot \left(\frac{\Delta L_x}{L_x} + \frac{\Delta L_y}{L_y} \right) \right]} \quad (3)$$

where L_x (L_y) is the theoretical length along the horizontal (vertical) axis, \bar{L}_x (\bar{L}_y) is the respective mean value for the printed geometry, and ΔL_x (ΔL_y) is its SD. After selecting the edges of the pores, the perimeter (μm) and the area (μm^2) to be used in Eq. 2 were measured by ImageJ.

In the view of cell experiments, after a crosslinking time from 0 to 30 min, five-layer grids (25 mm × 25 mm × 1.50 mm, 25% infill) were printed with P_{3.8}Ca₂₀Coll-DMEM HEPES at 10, 15 mm/s with 250 μm nozzles. After printing, grids were imaged and the results were compared to establish the optimal speed and crosslinking time for 3D-bioprinting.

2.2.4 Cell culture

SH-SY5Y human neuroblastoma cells (ATCC[®] code CRL-2266[™]), C8-D1A mouse astrocytes (ATCC[®] code CRL-2541[™]), and HOG human oligodendrogloma cells (EMD Millipore,

Merck, code SCC163) were grown in high-glucose DMEM (code 10938-025) supplemented with 10% v/v FBS, 2 mM L-glutamine, 100 U/ml penicillin and 100 µg/ml streptomycin sulfate. HMC3 human microglial cells (ATCC® code CRL-3304™) were grown in Advanced minimum essential medium (code 12492-013) supplemented with 10% v/v FBS and 2 mM L-glutamine. All cell lines were cultured at 37°C, 5% CO₂ in a humidified atmosphere. Medium was refreshed every two to 3 days and cells were split twice a week.

2.2.5 Indirect cytocompatibility: MTS assay

After preparation, P₄Ca₂₀-DMEM and P_{3,8}Ca₂₀Coll-DMEM were incubated with DMEM (code 10,938-025) supplemented with 10% v/v FBS, 2 mM L-glutamine, 100 U/ml penicillin and 100 µg/ml streptomycin sulfate. After 1, 4, 24, 72 h and 7 days, supernatants were replaced with fresh medium. Cells (62.50 × 10³ C8-D1A, HMC3, HOG/cm²; 93.75 × 10³ SH-SY5Y/cm²) were plated in 96-well plates. The following day, cells were incubated with the supernatants, while controls were cultured in standard medium. After 24 h, cell viability was evaluated by MTS assay. Supernatants were replaced with medium supplemented with 10% v/v MTS. After 3 h incubation, the optical density was measured at 490 nm (reference wavelength 630 nm) by a spectrophotometric plate reader (Infinite 200 PRO, Tecan, Männedorf, Switzerland). The results were normalized to those of the controls.

2.2.6 Microstructural characterization: Transmission electron microscopy

After mixing, samples (0.4 ml) were prepared into cylindrical molds (inner diameter: 11.05 mm) in 12-well plates. The procedure was repeated for cell-loaded constructs, obtained by mixing 2.5 × 10⁶ C8-D1A cells with collagen solution (9:1, volumetric ratio), and then with pectin/CaCO₃. The moulds were removed after 1 h.

The 3D organization of P_{3,8}Ca₂₀-DMEM and P_{3,8}Ca₂₀Coll-DMEM HEPES was evaluated by transmission electron microscopy (TEM, Tunesi et al., 2019). Samples were fixed in 2% glutaraldehyde in 0.1 M cacodylate buffer (pH 7.4) for 2 h, washed for several times in the same buffer, and post fixed in 1% osmium tetroxide for 1 h. After standard ethanol dehydration, specimens were embedded in Epon-Araldite 812 mixture. Ultrathin sections (80 nm thick) were obtained with a Reichert Ultracut S ultratome (Leica, Wien, Austria), placed on copper grids (300 mesh) and stained with uranyl acetate and lead citrate.

For the immunogold assay, cell-loaded samples were fixed in 4% p-formaldehyde and 0.5% glutaraldehyde in PBS for 2 h, and then dehydrated in ethanol series for resin embedding. Ultrathin sections were obtained as above and collected on gold grids (300 mesh). After etching with 3% NaOH in ethanol (Causton, 1984), sections were incubated for 30 min

in blocking solution containing 1% bovine serum albumin, 2% PBS and 0.1% Tween. They were incubated with the polyclonal primary antibody rabbit anti-COL1α1 (rabbit polyclonal, EMD Millipore) diluted 1:20 in blocking solution. After several washings in PBS, the primary antibody was visualized after immunostaining for 1 h with the secondary goat anti-rabbit IgG (H + L)-gold conjugate antibody (particle size: 10 nm. GE Healthcare, Amersham, UK) diluted 1:50 in blocking solution. In control experiments, the primary antibody was omitted, sections were treated with bovine serum albumin and incubated only with the secondary antibody. Sections were counterstained with uranyl acetate in water. Samples were observed with a Jeol 1010 EX electron microscope (Jeol, Tokyo, Japan) and data was recorded with a MORADA digital camera system (Olympus, Tokyo, Japan).

2.2.7 Direct cytocompatibility after 3D-bioprinting

Cells (2.5 × 10⁶ C8-D1A, HMC3, HOG; 3·10⁶ SH-SY5Y) were mixed to collagen solution (9:1, volumetric ratio), and then with pectin/CaCO₃. P_{3,8}Ca₂₀Coll-DMEM HEPES was loaded into a cartridge and kept in ice until assembling on the bioprinter. Five-layer grids were printed at 10 mm/s with 250 µm nozzles in 12-well plates after a crosslinking time from 10 to 20 min and covered with 0.75 ml medium.

After about 60 min crosslinking, cell viability following printing was assessed by a trypan blue exclusion assay. To view cells more easily, dissociation of the hydrogel network was promoted by incubation with sodium citrate (20 mM in DMEM (0.2% w/v), ~200 µL). An aliquot of cell suspension was mixed with trypan blue dye and counted with a Neubauer chamber. The percentage of live cells was calculated according to Eq. (4):

$$\text{live cells (\%)} = \frac{\sum_{i=1}^4 N^{\circ} \text{live cells}}{\sum_{i=1}^4 N^{\circ} \text{cells}} \cdot 100 \quad (4)$$

where 4 is the number of squares in which cells were counted and $N^{\circ} \text{ cells}$ is the total number of cells counted.

To stain cell nuclei of live and dead C8-D1A cells after bioprinting, samples were incubated for 10 min in fresh medium supplemented with 1 µM Hoechst 33342, 0.5 µM Calcein AM and 0.2 µM ethidium homodimer-1 dyes (ThermoFisher, Italy). Live fluorescence images were acquired by a confocal microscope (Ar1+, Nikon, Tokyo, Japan), equipped with an incubator chamber and four wavelength diode lasers ($\lambda_{\text{excitation}} = 405/488/561/640 \text{ nm}$). Stained cells were imaged with a ×10 objective, with 0.45 NA, 4WD. The pinhole was set to one Airy Unit. 1024 × 1024 pixels images were acquired as z-stack images. Samples were imaged with a 10 µm step, resulting in an acquisition depth of approximately 1.3000 µm.

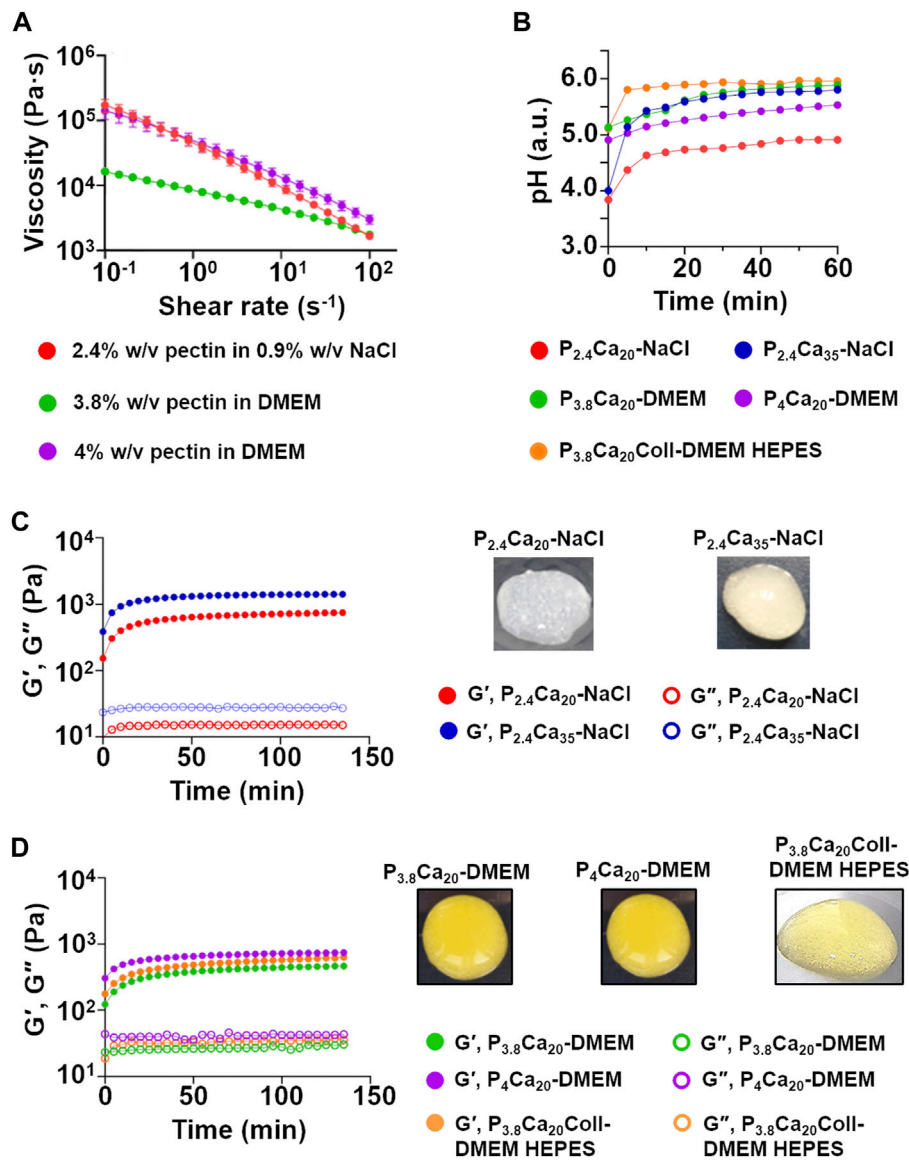


FIGURE 2

(A) Flow curves for 2.4% w/v pectin in 0.9% w/v NaCl, 3.8% w/v and 4% w/v pectin in DMEM. Mean \pm SD, 12 replicates/condition (B) pH of the tested materials as a function of crosslinking time. Mean values, three replicates/condition (C) G', G'' as a function of crosslinking time for $P_{2.4}Ca_{20}$ -NaCl and $P_{2.4}Ca_{35}$ -NaCl. Mean values, three replicates/condition. Representative images of both materials at 1 h (D) G', G'' as a function of crosslinking time for $P_{3.8}Ca_{20}$ -DMEM, P_4Ca_{20} -DMEM and $P_{3.8}Ca_{20}Coll$ -DMEM HEPES. Mean values, three replicates/condition. Representative images of the gels at 1 h.

To investigate the potential of $P_{3.8}Ca_{20}Coll$ -DMEM HEPES for 3D-bioprinted models of brain tissue, cell constructs were printed in Transwell® permeable supports in 6-multiwell plates. After 60 min crosslinking, they were covered with 2.5 ml culture medium. On 1, 4, 24 h, 3 and 7 days, cell viability was evaluated by a resazurin assay. Samples were maintained in cell culture medium

supplemented with 10% v/v resazurin 0.2 mg/ml in PBS for 3.5 h, then 100 μ L supernatants were moved to a 96-well plate and fluorescence was measured at 560 nm (reference wavelength 590 nm, manual gain: 60) by a spectrophotometric plate reader. The analyses were also performed on cell-free samples, whose fluorescence was subtracted from the cell-loaded ones.

2.2.8 Statistical analysis

Results were reported as mean \pm SD and analyzed with GraphPad Prism[®], release 9 (GraphPad Software, La Jolla, CA, United States). The normality of data distribution was assessed by D'Agostino & Pearson test. For comparisons among groups, one-way analysis of variance (ANOVA) followed by Tukey's multiple comparison test was performed. For comparisons between two groups, a two-tailed Mann-Whitney test was applied. Differences were considered as statistically significant when p -value <0.05 (*).

3 Results

In this study, we exploited the potential of a well-defined set of rheological analyses to study the viscoelastic properties of pectin solutions and gels. Our results predicted ink printability and expanded the 3D-reactive printing approach (Sardelli et al., 2021) by controlling both on printing time and pH. Both parameters were also fundamental to lay the grounds towards the development of pectin-based formulations as novel inks for 3D-bioprinting in neural tissue engineering-related applications.

3.1 Rheological characterization and pH measurements

Pectin solutions exhibited a shear thinning behavior, independently of the solvent adopted (Figure 2A). In agreement with other studies (Kar and Arslan, 1999; Moreira et al., 2014), viscosity depended both on pectin concentration and pH. At all shear rates, viscosity was greater for 4% w/v than 3.8% w/v pectin in DMEM. At low shear rates, the flow curves for 2.4% w/v pectin in 0.9% w/v NaCl and 4% w/v pectin in DMEM were overlapping.

As previously suggested, pH regulation is fundamental to prevent metabolic alterations, maintain cell viability and exert signaling (Chesler, 2003; Flinck et al., 2018). However, the acidic pH of pectin solutions and hydrogels could limit their use for cell delivery (Moreira et al., 2014). For these reasons, pH was monitored over crosslinking time (Figure 2B). At all the time points, the higher amount of CaCO₃ (35 mM) led to a faster increase of pH, producing hydrogels with a stiffer consistency (Figure 2C), but with residual deposits of calcium salts (e.g. for P_{2.4}Ca₂₀-NaCl, pH = 4.37 at 5 min and pH = 4.91 at 1 h; while 35 mM CaCO₃ induced pH = 5.14 at 5 min and pH = 5.80 at 1 h). Dissolving pectin in DMEM (i.e. a buffered solution) was advantageous only in the first time point (at 5 min, for P_{2.4}Ca₂₀-NaCl pH = 4.37. In the presence of DMEM, pH = 5.26, Figure 2B). The addition of HEPES and Coll increased the pH both at shorter and longer time points (for P_{3.8}Ca₂₀Coll-DMEM HEPES, pH = 5.81 at 5 min and pH = 5.97 at 1 h). Although small, these differences are fundamental. When

external pH is lowered from physiological values, cell membranes are deformed, processes stop moving or are retracted, cytoplasmic components start aggregating, and mitosis is paused. How long cells can withstand this condition depends on the acidity of the environment, but for pH values close to 6, slight differences (e.g. ~ 0.3 pH units) can extend this time of some hours (Taylor, 1962).

The different composition and pH values affect the crosslinking kinetics, as was observable by time sweeps (Figures 2C, D). For all the materials, a solid-like state ($G' > G''$) was observed from $t = 0$, indicating that gelation occurred before starting the scans. P_{2.4}Ca₃₅-NaCl showed the highest viscoelastic properties (at the end of the scans, $G' = 1.41 \cdot 10^3$ Pa; $G'' = 0.27 \cdot 10^3$ Pa). G' , but for some materials also G'' , increased over time, suggesting that crosslinking continued over time and gels progressively stiffened, in agreement with previous studies (Secchi et al., 2014). After a rapid rise in the first 15 min, the increase in stiffening slowed down and it was noticeable only over longer time frames. After 1 h, G' was equal to 80%–90% of its value at 140 min, when crosslinking could be considered as complete. In contrast, G'' did not vary or only slightly varied over time. At 3.8% w/v pectin concentration, DMEM reduced the crosslinking rate and collagen did not affect it. Based on these results and to identify a relevant time window for extrusion-based bioprinting, we set 60 min crosslinking as the threshold value to study hydrogel properties. Indeed, since 3D-bioprinting experiments were not performed inside a cell culture incubator (i.e. it was not possible to control the temperature, humidity and carbon dioxide concentration to maintain an optimal environment for cell growth), cell viability could not be ensured (the latter can only be ensured if cells are kept out of an incubator for short time frames).

Since extrusion-based printing requires the inks to flow through the nozzle/needle, their extrudability was studied (Figures 3A–C). As previously reported, the commonly accepted rheological indicator of extrudability is the viscosity, with higher viscosity leading to lower extrudability (Copus et al., 2022). Extrudability increased with the shear rate. In agreement with the rapid rise in dynamic moduli in the initial crosslinking phases, for a fixed shear rate extrudability at 0 min was greater than at 30 min, while the differences between 30 min and 60 min were negligible. At low shear rates, after 0 and 30 min crosslinking, P_{3.8}Ca₂₀Coll-DMEM HEPES showed the highest extrudability, while hydrogels in 0.9% w/v NaCl exhibited the lowest. At high shear rates, no difference was observed. To account for the influence of crosslinking kinetics, only the flow curves at 60 min were fitted with the power law model of Ostwald and de Waele (Eq. 5):

$$\eta = K(\dot{\gamma})^{n-1} \quad (5)$$

where η is the viscosity, K the consistency index, $\dot{\gamma}$ the shear rate and n the power law index. n ranges from 0 to 1, with one

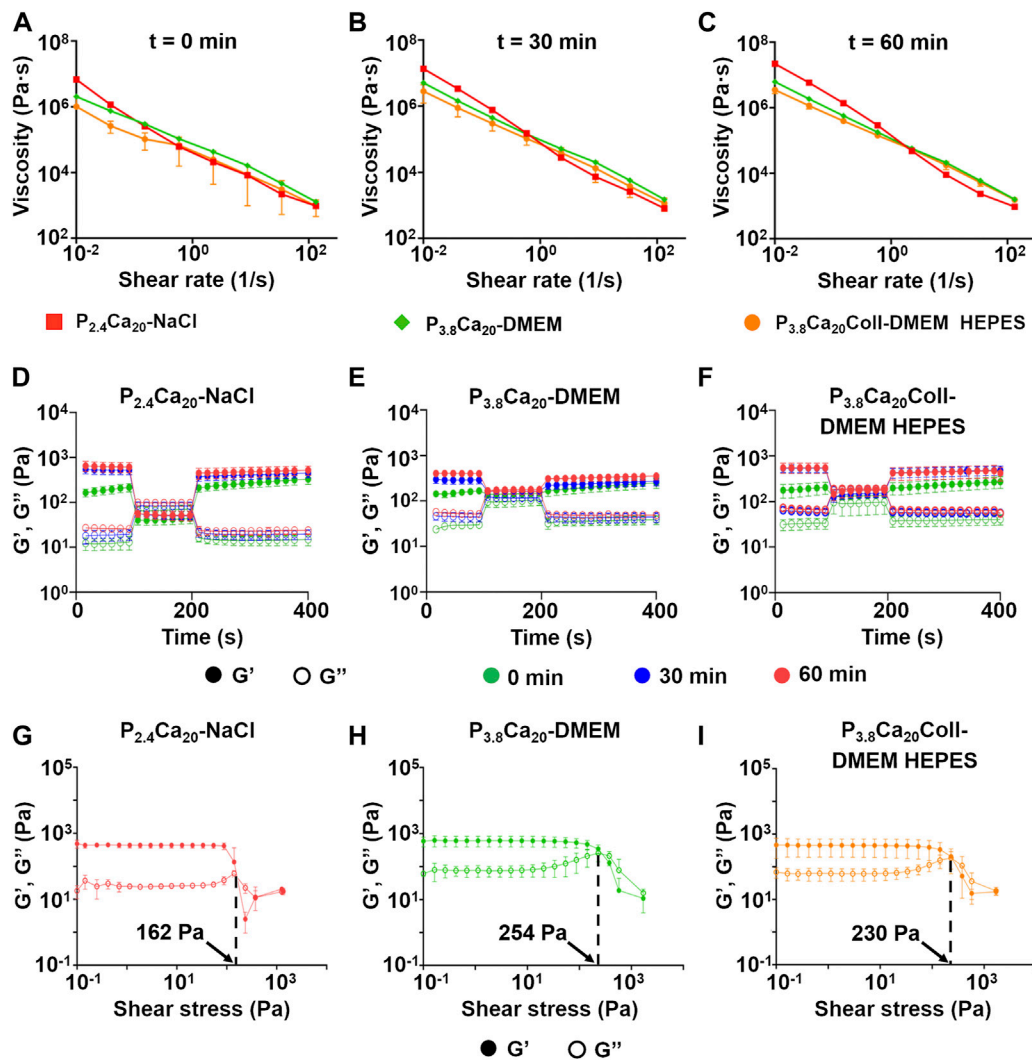


FIGURE 3

Prediction of ink extrudability from the flow curves at 0 (A), 30 (B), and 60 (C) min crosslinking for $P_{2.4}Ca_{20}$ -NaCl, $P_{3.8}Ca_{20}$ -DMEM, and $P_{3.8}Ca_{20}$ Coll-DMEM HEPES. Mean \pm SD, 4 replicates/condition; Recovery of G' , G'' as a function of test time for $P_{2.4}Ca_{20}$ -NaCl (D), $P_{3.8}Ca_{20}$ -DMEM (E), and $P_{3.8}Ca_{20}$ Coll-DMEM HEPES (F) after applying a 100% strain at 1 Hz for 100 s. Mean \pm SD, 4 replicates/condition. G' and G'' over shear stress after 60 min crosslinking for $P_{2.4}Ca_{20}$ -NaCl (G), $P_{3.8}Ca_{20}$ -DMEM (H), and $P_{3.8}Ca_{20}$ Coll-DMEM HEPES (I). The arrows indicate the yield stress. Mean \pm SD, three replicates/condition.

corresponding to a Newtonian (shear rate-independent) viscosity (Supplementary Table S1). As K rises, viscosity increases. Lower K , n values are related to a greater ease of extrusion and potentially to lower printing pressures (Liu et al., 2019). Although in disagreement with the printability results (see the following section), the lowest K , n values were calculated for $P_{2.4}Ca_{35}$ -NaCl ($K=6.50 \times 10^4$, $n=7.8 \times 10^{-3}$). However, in support of the potential of this formulation for extrusion-based printing, the second lowest value of K was computed for $P_{3.8}Ca_{20}$ Coll-DMEM HEPES ($K=8.39 \times 10^4$). Moreover, for

gels in cell culture medium, $n > 0.1$; while for the ones in 0.9% w/v NaCl, $n < 0.01$. We hypothesized that in the first situation (e.g. 20 mM $CaCO_3$, DMEM and collagen) the power law was able to accurately model hydrogel behavior and to validate the shear thinning behavior, while in the second one (e.g., 35 mM $CaCO_3$, 0.9% w/v NaCl) the extremely low value of n , if not related to a slippage between the rheometer plates, indicated a plug flow in the nozzle of the printer, rather than the flow of a liquid (Lopez Hernandez et al., 2021)

TABLE 2 G' Recovery, G'' Recovery, and $\tan(\delta)_{150}$ for the proposed inks. They were calculated according to Eqs 6–8. The measurements were carried out at 0, 30, and 60 min crosslinking. Mean values, 4 replicates/condition.

Time (min)	Ink	G' Recovery	G'' Recovery	$\tan(\delta)_{150}$
0	$P_{2.4}Ca_{20}$ -NaCl	+52%	+14%	1.64
30		-14%	+2%	1.63
60		-15%	-6%	1.87
0	$P_{2.4}Ca_{35}$ -NaCl	+22%	+19%	4.03
30		-15%	-11%	3.59
60		-12%	-2%	3.94
0	P_4Ca_{20} -DMEM	+44%	+29%	1.00
30		—	+1%	1.20
60		-5%	-2%	1.17
0	$P_{3.8}Ca_{20}$ -DMEM	+48%	+29%	0.70
30		-6%	—	0.70
60		-12%	-5%	0.91
0	$P_{3.8}Ca_{20}$ Coll-DMEM HEPES	+33%	+22%	0.69
30		-9%	-3%	1.25
60		-24%	-16%	1.09

After 0, 30, and 60 min crosslinking, G' and G'' recovery was calculated (Figures 3D–F and Table 2) according to Eqs. 6 and 7, respectively; after applying a 100% strain for 100 s:

$$G'_{\text{Recovery}} (\%) = \left(\frac{G'_{400}}{G'_{100}} \right) \cdot 100 - 100 \quad (6)$$

$$G''_{\text{Recovery}} (\%) = \left(\frac{G''_{400}}{G''_{100}} \right) \cdot 100 - 100 \quad (7)$$

where G'_{400} (G''_{400}) is G' (G'') value at 400 s (i.e. at the end of the test) and G'_{100} (G''_{100}) is G' (G'') value at 100 s (i.e. before applying a 100% strain for 100 s). To assess whether a deformation beyond the LVR affects hydrogel structure, at 150 s after beginning the test, $\tan(\delta)$ was calculated according to Eq. 8:

$$\tan(\delta)_{150} = G''_{150} / G'_{150} \quad (8)$$

where G'_{150} (G''_{150}) is G' (G'') value at 150 s.

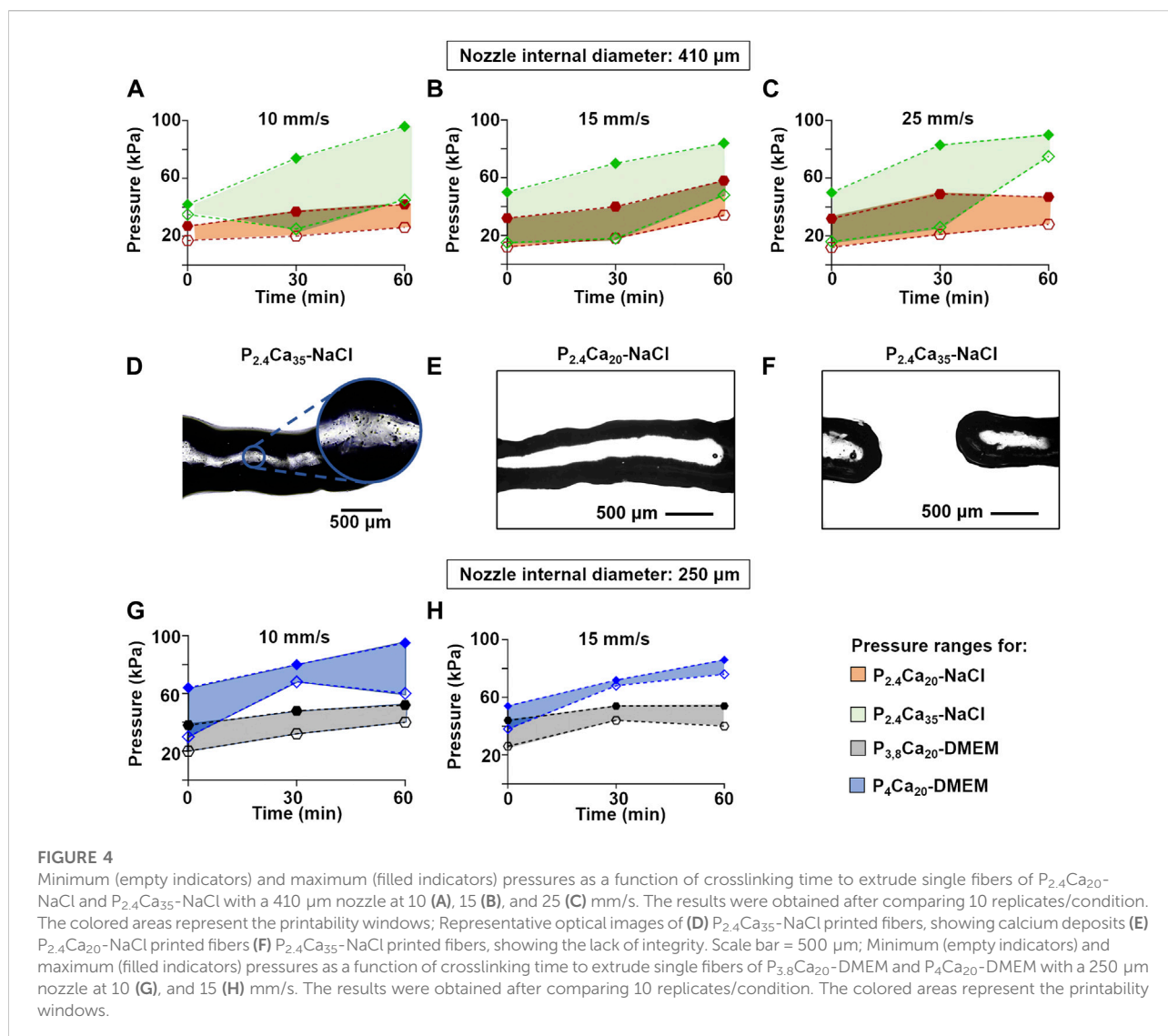
When gels were subjected to an increasing shear immediately after preparation ($t = 0$), they not only recovered, but they even increased their viscoelastic properties (maximum values were about 50% for G' and about 30% for G''). The situation changed after 30 min crosslinking: except for P_4Ca_{20} -DMEM (no changes), G' values did not recover after the deformation for the considered hydrogels. At this time point G'' values were constant or only slightly modified. After 60 min crosslinking, the

inks did not recover their viscoelastic properties. $P_{3.8}Ca_{20}$ Coll-DMEM HEPES showed the highest decrease in G' (-24%) and G'' (-16%) values.

At all the crosslinking time points, $\tan(\delta)_{150}$ was > 1 (liquid-like state) for inks in 0.9% w/v NaCl, while $\tan(\delta)_{150}$ was < 1 for DMEM samples w/o collagen, indicating a solid-like state. For the other materials, $\tan(\delta)_{150}$ depended on crosslinking time. At 0 min, for P_4Ca_{20} -DMEM the deformation triggered a solid-to liquid-like transition ($\tan(\delta)_{150} = 1$), while $P_{3.8}Ca_{20}$ Coll-DMEM HEPES maintained its solid-like behavior. At 30 min and 60 min, both the materials showed a liquid-like behavior. At 60 min, for $P_{3.8}Ca_{20}$ Coll-DMEM HEPES, $\tan(\delta)_{150}$ decreased and approached to 1 (1.09).

For shear stresses larger than the yield stress (Figures 3G–I), G'' was higher than G' and the sample started flowing. Therefore, the presence of a yield stress indicated that the hydrogel was capable to be extruded during printing.

Taken together, these results demonstrate that all the hydrogels efficiently recovered their viscoelastic properties when exposed to a strain beyond the LVR immediately after preparation, because in the early phases of crosslinking the general increase in dynamic moduli was fast. In agreement with the measured values of yield stress, the materials in cell culture medium required a higher deformation for a solid-to liquid-like transition. Between 30 and 60 min crosslinking, the rise in dynamic moduli during the recovery phase was considerably reduced and it could not compensate the effects



of an extreme deformation. Except for $P_{3.8}Ca_{20}$ -DMEM, all the formulations behaved as liquids, at the end of the recovery period. The exceptional behaviour of $P_{3.8}Ca_{20}$ -DMEM could be explained by the fact that this formulation exhibited the greatest yield stress. The addition of collagen to $P_{3.8}Ca_{20}$ -DMEM lowered the yield stress and improved the extrudability, with advantages for 3D-bioprinting.

3.2 Printability evaluation

Since cell printing with high viscous inks (i.e. in hydrogels with high polymer content) requires high pressures and printing pressure can impair cell viability (Cidonio et al., 2019; Boulaoui et al., 2020), we studied the influence of speed and crosslinking on printing pressure (Figure 4).

The effect of $CaCO_3$ content was investigated by printing a series of single fibers for $P_{2.4}Ca_{20}$ -NaCl and $P_{2.4}Ca_{35}$ -NaCl, i.e. for inks with the same pectin concentration (2.4% w/v) dissolved in the same solvent (0.9% w/v NaCl), but with different calcium content (20 or 35 mM) (Figures 4A–C). At a fixed speed, both minimum and maximum pressures increased over crosslinking time. At a fixed crosslinking time, $CaCO_3$ content affected maximum pressures. The higher amount of $CaCO_3$ led to a greater gap between minimum and maximum pressures and required higher maximum pressures for extrusion. In contrast, comparable minimum pressures could be set at 0 min when printing at 15 or 25 mm/s, and at 30 min independently of speed. For a fixed $CaCO_3$ content, pressures varied with speed. For $P_{2.4}Ca_{35}$ -NaCl, fibers could be extruded at lower pressures when printing at 15 mm/s, while for $P_{2.4}Ca_{20}$ -NaCl when printing at 10 or 15 mm/s. Since for both inks printing at 25 mm/s required

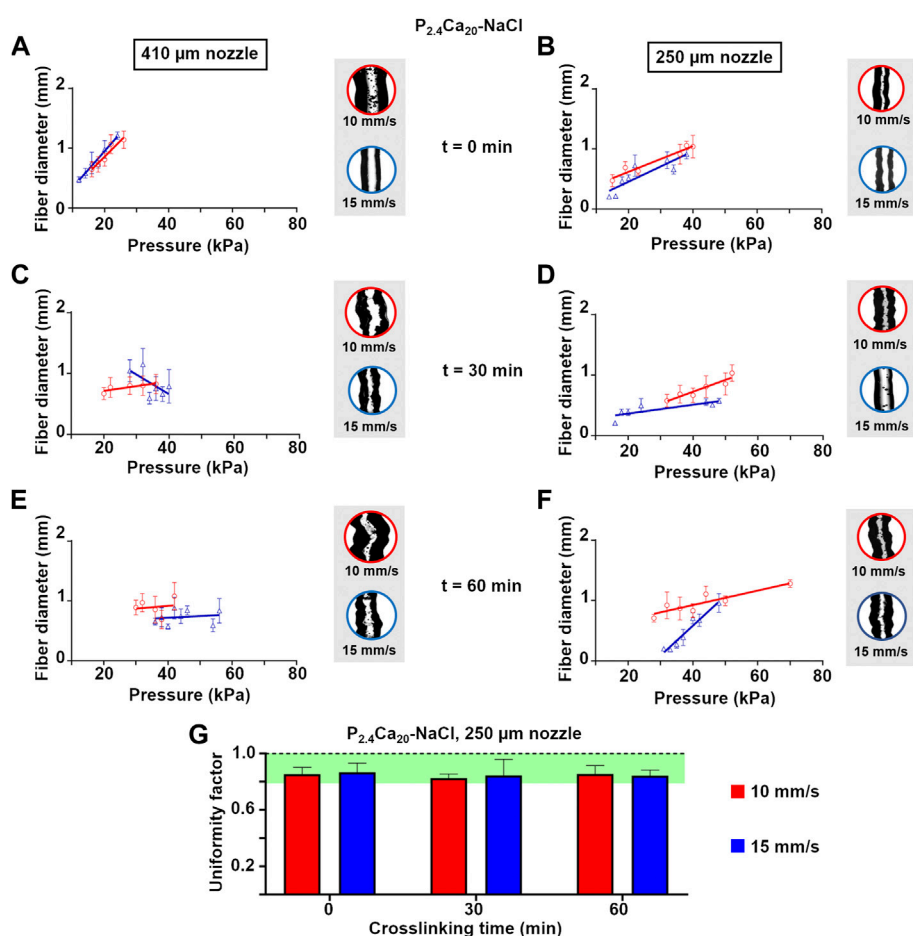


FIGURE 5

Fiber diameter as a function of printing pressure for $P_{2.4}Ca_{20}$ -NaCl single fibers extruded with a 410 or 250 μm nozzle at 10 or 15 mm/s after 0 (A and B), 30 (C and D), and 60 (E and F) min crosslinking. Mean \pm SD, six replicates/condition. For each condition, representative optical images of the central part of the fibers were reported (G) Uniformity factor (U) for $P_{2.4}Ca_{20}$ -NaCl single fibers extruded with a 250 μm nozzle at 10 or 15 mm/s after 0, 30, and 60 min crosslinking. Mean \pm SD, six replicates/condition.

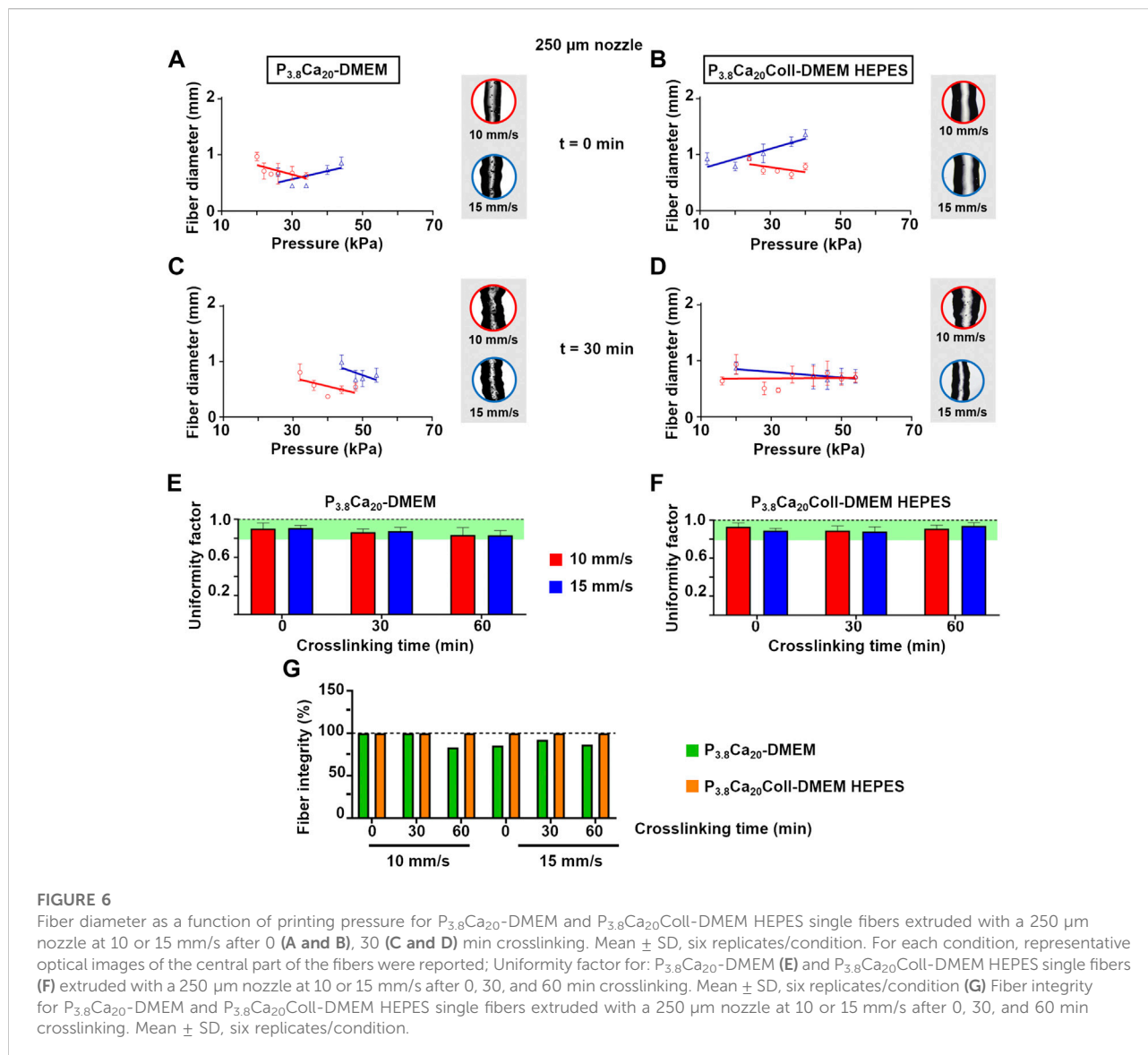
pressures comparable or greater than printing at 10 or 15 mm/s, we excluded the fastest speed.

The microscopic observation of fibers with the higher calcium content (35 mM) highlighted dark spots (Figure 4D), indicating deposits of calcium carbonate. For both inks, fiber integrity decreased over crosslinking time and $CaCO_3$ concentration (data not shown). Moreover, $P_{2.4}Ca_{35}$ -NaCl frequently clogged the nozzle, requiring the interruption of the process (Figures 4E, F).

The effect of pectin concentration was investigated by printing a series of single fibers for P_4Ca_{20} -DMEM and $P_{3.8}Ca_{20}$ -DMEM, i.e. for inks with the same calcium content (20 mM), but with different pectin contents (4% or 3.8% w/v) dissolved in the same solvent (DMEM) (Figures 4G, H). As for inks in 0.9% w/v NaCl, at a fixed speed, both minimum and maximum pressures increased over crosslinking time. Although there were only slight differences compared to inks in 0.9% w/v NaCl, at a fixed

crosslinking time, pectin concentration affected both minimum and maximum pressures, with the extrusion of P_4Ca_{20} -DMEM requiring higher pressures than $P_{3.8}Ca_{20}$ -DMEM. The printing speed also affected the results: for $P_{3.8}Ca_{20}$ -DMEM, pressure values were lower when extruding at 10 mm/s than 15 mm/s; while for P_4Ca_{20} -DMEM lower values were set when printing at 15 mm/s.

The influence of pressure and speed on fiber diameter was related to the print resolution. At the beginning of crosslinking (0 min), the diameter of printed $P_{2.4}Ca_{20}$ -NaCl fibers increased with pressure both at 10 or 15 mm/s (Figure 5A). After 30 min crosslinking (Figure 5C), pressure induced a change in diameter only at 10 mm/s. When crosslinking time reached 60 min, the shape was retained regardless of pressure (Figure 5E). Independently of speed, fibers were always larger than the nozzle for the minimum printing pressures (Supplementary Table S2). When the nozzle dimension was reduced from



410 μm to 250 μm (Figures 5B, D, F), fiber diameter (Supplementary Table S2) increased (or slightly increased) with increasing pressure, independently of crosslinking time. More specifically, the speed of 15 mm/s allowed to extrude $P_{2.4}Ca_{20}$ -NaCl fibers thinner than the nozzle and with a basically constant diameter (\sim about 205 μm , mean value) from 0 to 60 min crosslinking.

Generally, printing through the smaller nozzle (250 μm) produced thinner fibers. Surprisingly, minimum pressures were generally comparable or even lower than the ones for extrusion through the larger nozzle. This result agrees with the shear thinning nature of $P_{2.4}Ca_{20}$ -NaCl: a reduction in nozzle dimension, increases the shear strain, and decreases the viscosity, thus reducing printing pressure. For this reason, we selected 250 μm nozzles for further 3D-printing experiments.

The uniformity factor is an important parameter to compare the geometrical features of the set with the experimental results after printing. For $P_{2.4}Ca_{20}$ -NaCl fibers extruded through 250 μm nozzles, the uniformity factor was always greater than 0.82 (Figure 5G). For all the crosslinking times, no differences (p -value $>$ 0.05) were found between 10 and 15 mm/s. The comparison of mean values showed greater uniformity factors for printing at 15 mm/s at both 0 and 30 min crosslinking. However, at this printing speed a lower number of fibers was available for the analysis. Indeed, when printing at 10 mm/s fiber integrity was greater than 90%; while it dropped to 50% in the tests at 15 mm/s (data not shown).

For DMEM-based hydrogels either with or without collagen (i.e. $P_{3.8}Ca_{20}$ -DMEM and $P_{3.8}Ca_{20}Coll$ -DMEM HEPES, respectively), pressure and speed influenced fiber diameter

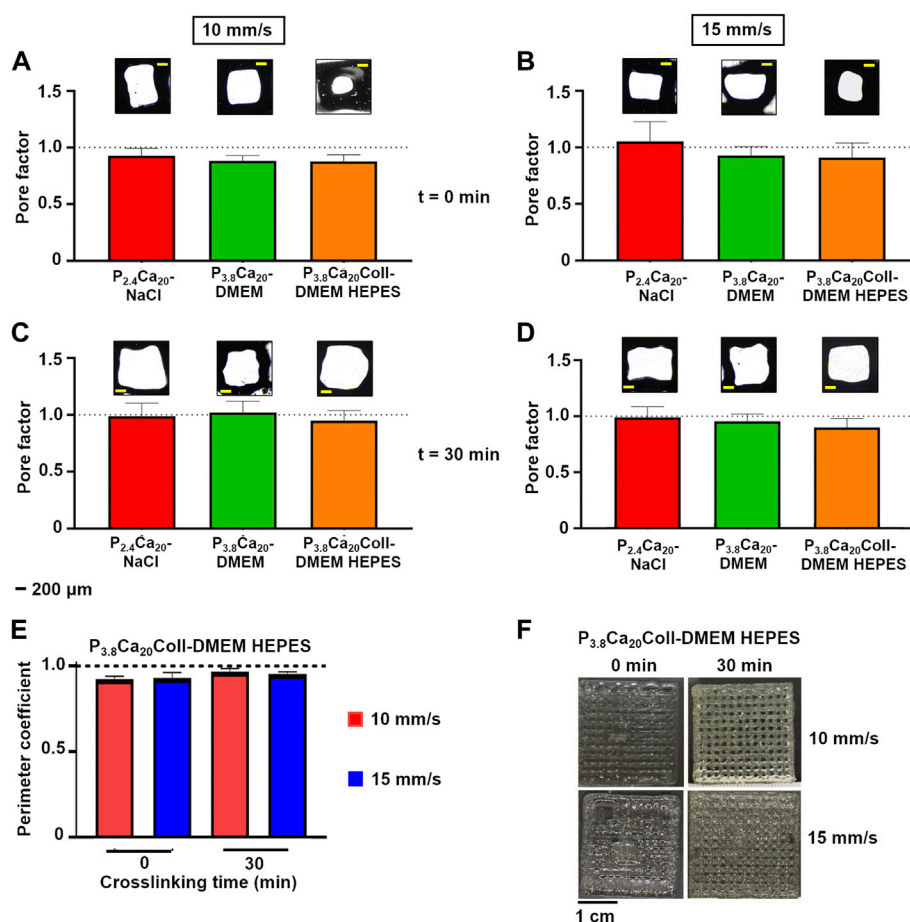


FIGURE 7

Pore factor for $P_{2.4}Ca_{20^-}NaCl$, $P_{3.8}Ca_{20^-}DMEM$ and $P_{3.8}Ca_{20}Coll-DMEM HEPES$ two-layer geometries printed after 0 and 30 min crosslinking at 10 (A and B) or 15 (C and D) mm/s. For each condition, representative optical images of the pores were reported. Scale bar = 200 μm (E) Perimeter coefficient for $P_{3.8}Ca_{20}Coll-DMEM HEPES$ two-layer geometries printed after 0 and 30 min crosslinking at 10 or 15 mm/s (F) Representative images of five-layer grids printed after 0 and 30 min crosslinking at 10 or 15 mm/s. Scale bar = 1 cm.

(Figure 6, Supplementary Table S2). At 0 min (Figures 6A, B), the trends depended on speed, but not on the presence of collagen. For both inks, when printing at 10 mm/s, diameter decreased with increasing pressure, while the opposite was observed when printing at 15 mm/s. At 30 min, the trends were influenced by the presence of collagen. In the absence of collagen (i.e. for $P_{3.8}Ca_{20^-}DMEM$), diameter decreased with increasing pressure, while in the presence of collagen (i.e. for $P_{3.8}Ca_{20}Coll-DMEM HEPES$), it was basically independent of pressure and speed (Figures 6C, D). At 60 min crosslinking, the trends varied with both speed and the presence of collagen. In the absence of collagen, when extruding at 10 mm/s, diameter increased with increasing pressure, while when printing at 15 mm/s, the opposite was observed (data not shown). Again, in the presence of collagen, the diameter of printed fibers was basically independent of pressure and speed (data not shown).

For crosslinking times compatible with cell viability outside the incubator during the printing process (i.e. 0 and 30 min), $P_{3.8}Ca_{20}Coll-DMEM HEPES$ was extruded at lower pressures than $P_{3.8}Ca_{20^-}DMEM$, thus representing an advantage for cell viability. The shift from 0.9% w/v NaCl to DMEM lowered print resolution, although the fibers were smoother and straighter. The addition of collagen to DMEM-based formulations improved fiber uniformity (Figures 6E, F), and integrity (Figure 6G). By extending the analysis up to 60 min, we were able to appreciate that collagen also improved recovery as crosslinking time increased. In fact, for $P_{3.8}Ca_{20^-}DMEM$ fibers extruded at both 10 mm/s and 15 mm/s, the uniformity factors decreased from 0.91 (0 min) to 0.87 (30 min) and 0.83 (60 min), while for $P_{3.8}Ca_{20}Coll-DMEM HEPES$ fibers, they decreased from 0.91 (0 min) to 0.88 (30 min) and then increased to 0.92 (60 min).

TABLE 3 Pressure ranges for printing $P_{2.4}Ca_{20}$ -NaCl, $P_{3.8}Ca_{20}$ -DMEM, and $P_{3.8}Ca_{20}$ Coll-DMEM HEPES two-layered geometries with a 250 μ m nozzle. Mean values, six replicates/condition.

Ink	Speed (mm/s)	Time (min)	Minimum pressure (kPa)	Maximum pressure (kPa)
$P_{2.4}Ca_{20}$ -NaCl	10	0	15	40
		30	32	68
	15	0	18	30
		30	22	57
$P_{3.8}Ca_{20}$ -DMEM	10	0	22	31
		30	32	62
	15	0	20	35
		30	44	74
$P_{3.8}Ca_{20}$ Coll-DMEM HEPES	10	0	20	27
		30	27	42
	15	0	9	32
		30	17	41

As a proof of concept that it is possible to fabricate 3D-controlled shapes, we produced multilayered grids. As the uniformity factors did not allow for a unique selection of the printing speed, two-layer geometries were printed at different speeds and crosslinking times (Figures 7A–D). The minimum pressure values were set according to the ones for single fibers, but pressure could be increased during extrusion to allow for a continuous flow (Table 3). At 0 min, $P_{2.4}Ca_{20}$ -NaCl grids were more uniform when printed at 10 mm/s than 15 mm/s (p -value<0.01); while at 30 min no differences were found with speed (p -value>0.05). More in general, the most uniform grids were printed at 10 mm/s after 30 min crosslinking ($P_r = 0.99 \pm 0.09$). In these conditions, pores were the largest (i.e. fibers were the thinnest). For $P_{3.8}Ca_{20}$ -DMEM, the results were reversed: at 0 min, no differences were found with speed (p -value>0.05); while at 30 min grids were more uniform when printed at 10 mm/s (p -value<0.05). Accordingly, for this ink the most uniform grids ($P_r = 1.01 \pm 0.14$) were printed at 10 mm/s after 30 min crosslinking, and larger pores were obtained at the same crosslinking time when printing at 15 mm/s. However, when printing at 10 mm/s P_r increased with time (p -value<0.0001), whereas no differences were found with time at 15 mm/s (p -value>0.05). Even though for both crosslinking times no differences were found with speed (p -value>0.05), also for $P_{3.8}Ca_{20}$ Coll-DMEM HEPES the most uniform grids were printed at 10 mm/s after 30 min crosslinking ($P_r = 0.95 \pm 0.09$, mean \pm SD). Again, an increase in the mean values of P_r (from 0.88 to 0.93) was observed over time at 10 mm/s. As regards P_e (Figure 7E), at both crosslinking times, no differences were found with speed

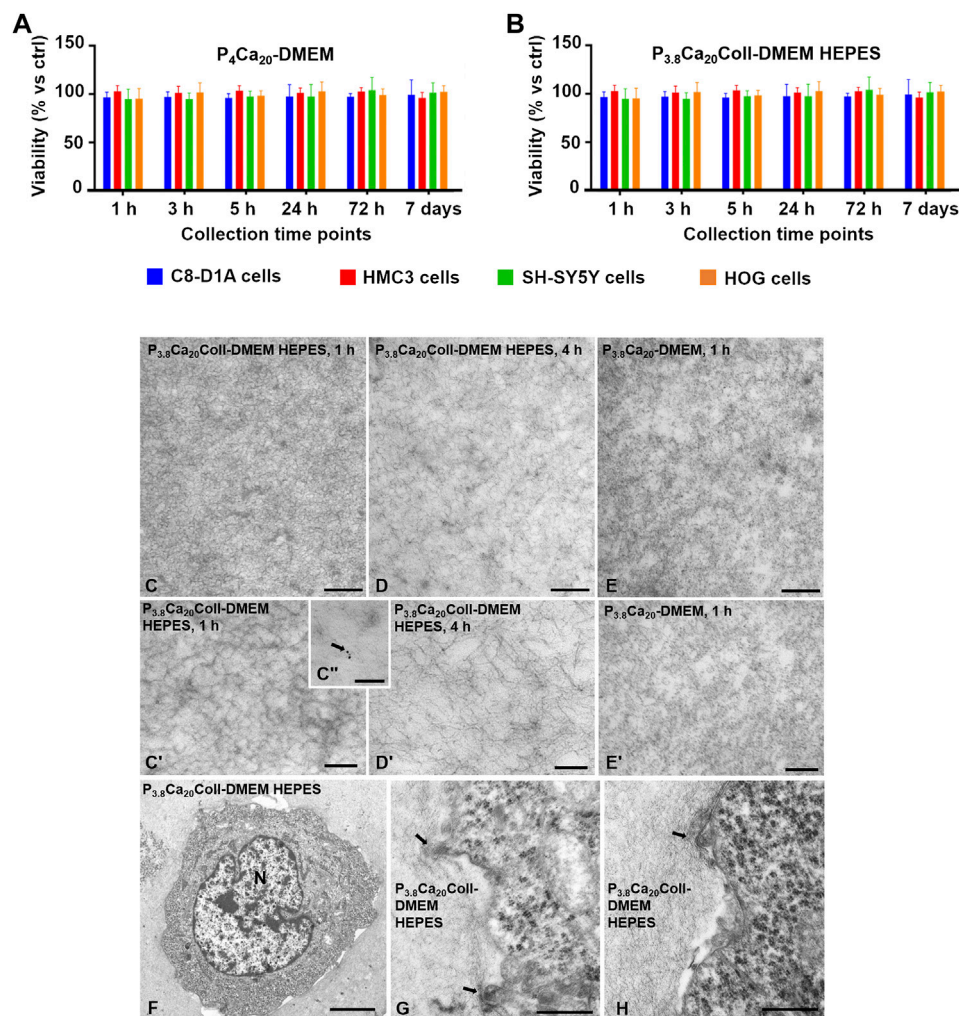
(p -value>0.05). After 30 min crosslinking, it increased for both types of grids, independently of speed.

Finally, we printed $P_{3.8}Ca_{20}$ Coll-DMEM HEPES five-layer-grids (Figure 7F). Unlike the two-layer geometries, the speeds were not equivalent. For both crosslinking times, more uniform fibers and open porosities were obtained at 10 mm/s, but the shape fidelity increased over time.

Based on the results observed, we selected a crosslinking time between 10 and 20 min as the ideal printing time, and 10 mm/s as the ideal printing speed. They represented a compromise between the values of pore factor (P_r , related to shape fidelity) and printing pressures (influencing cell viability, see the following section). Each five-layer-grid required about 100 s to be completed.

3.3 Indirect cytocompatibility: MTS assay

The effect of both pectin and collagen concentrations on cell viability was investigated by culturing the cells for 24 h in the supernatants from P_4Ca_{20} -DMEM (Figure 8A) or $P_{3.8}Ca_{20}$ Coll-DMEM HEPES (Figure 8B). As they were not specifically developed for cell encapsulation, we neglected 0.9% w/v NaCl-based compositions and tested DMEM-based formulations. We considered a pectin concentration of 4% w/v because it is the highest that has been tested in this study, and the pH values in the first crosslinking phases were than the ones for $P_{3.8}Ca_{20}$ -DMEM (Figure 2). We hypothesized that P_4Ca_{20} -DMEM is cytocompatible with SH-

**FIGURE 8**

Viability of C8-D1A, HMC3, SH-SY5Y and HOG cells after 24 h in the supernatants collected after 1, 3, 5, 24, 72 h, and 7 days from P_4Ca_{20} -DMEM (A), and $P_{3.8}Ca_{20}Coll$ -DMEM HEPES (B) hydrogels. As a control, cells were grown for 24 h in fresh culture medium. Results from the MTS assay. Mean \pm SD, 12 replicates/group. Data was analyzed with one-way ANOVA followed by Tukey's multiple comparisons test. All the differences were not statistically significant (p -value >0.05). TEM images of $P_{3.8}Ca_{20}Coll$ -DMEM HEPES after 1 h (C, C') and 4 h (D, D') crosslinking, and $P_{3.8}Ca_{20}$ -DMEM after 1 h (E, E') crosslinking, showing that in $P_{3.8}Ca_{20}Coll$ -DMEM HEPES, collagen fibers were crosslinked together forming a dense network, while in $P_{3.8}Ca_{20}$ -DMEM a uniform-looking matrix was present. Immunogold assays highlighted the specific localizations of gold particles associated to collagen fibers (arrow in C'). C8-D1A astrocytic-like cells seeded in $P_{3.8}Ca_{20}Coll$ -DMEM HEPES (F) showed contact and interacted with collagen fibers (arrows in (G, H)). N, nucleus. Bars in C-E, G, and H are 0.5 μ m; bars in C' and D' are 200 nm; bar in C'' is 100 nm; bar in F is 5 μ m.

SY5Y, C8-D1A, HMC3, and HOG cells, any similar pectin gel is expected to be too, but with a lower pectin concentration. For all the collection times and cell populations, viability, which was evaluated by MTS, was comparable with controls in standard medium (p -value >0.05). Although the crosslinking reaction is still not complete, culture medium can be immediately added to cover the samples and its addition speeds up the reaching of pH values compatible with cell survival. The selected collagen content did not reduce cell viability. Again, for all the cell

populations, viability was comparable with controls for all the time points (p -value >0.05).

3.4 Microstructural characterization: Transmission electron microscopy

Ultrastructural analysis by TEM of cell-embedding samples fixed after 60 min (Figures 8C,C') or 4 h culture (Figures 8D,D')

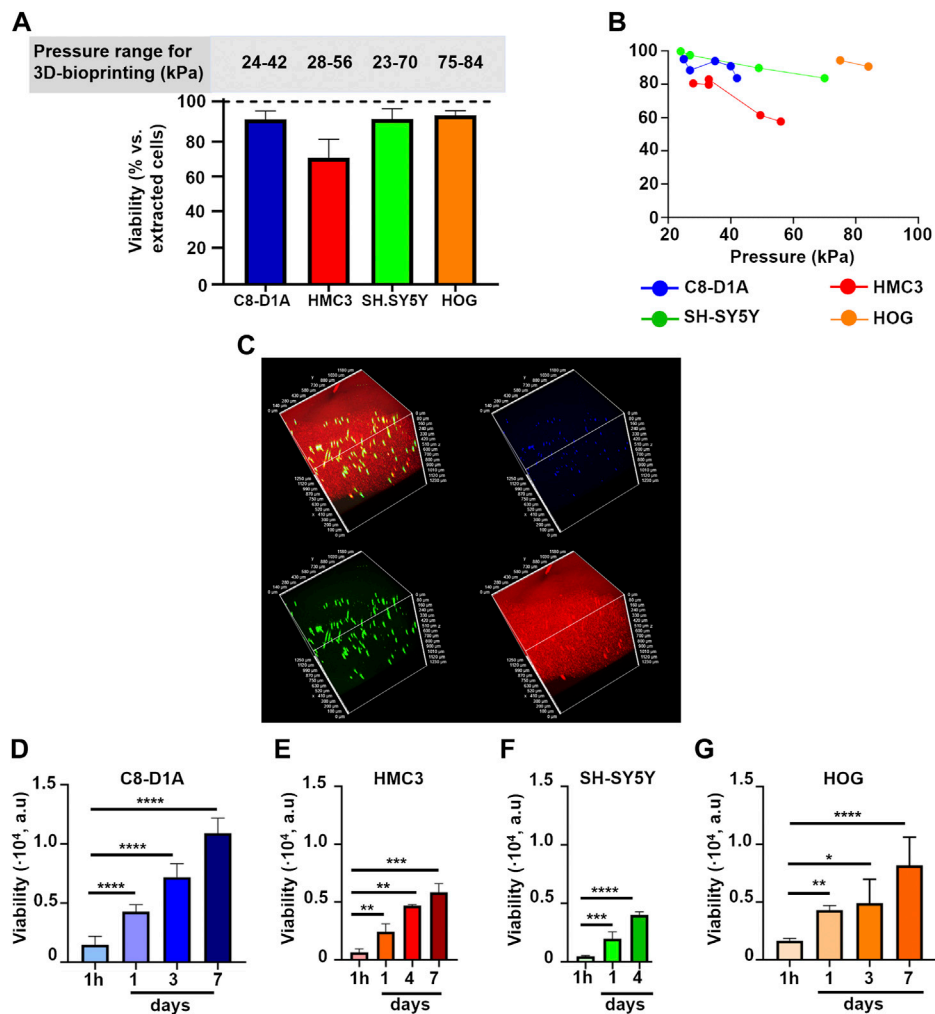


FIGURE 9

(A) Percentage of live cells with respect to the total number of counted cells after dissociating $P_{3.8}Ca_{20}Coll$ -DMEM HEPES constructs. Results from the trypan blue exclusion assay for C8-D1A, HMC3, SH-SY5Y, and HOG cells. Mean \pm SD, at least six replicates/condition. The upper panel shows the pressure ranges to print the constructs (B) Percentage of live cells with respect to the total number of counted cells after dissociating $P_{3.8}Ca_{20}Coll$ -DMEM HEPES constructs as a function of printing pressure. Each point on the graph represents the average of three constructs printed consecutively. Results from the trypan blue exclusion assay for C8-D1A, HMC3, SH-SY5Y, and HOG cells (C) 3D reconstruction of C8-D1A cells 3D-bioprinted in $P_{3.8}Ca_{20}Coll$ -DMEM HEPES. Viable cells were stained green, while cell nuclei were stained blue. $P_{3.8}Ca_{20}Coll$ -DMEM HEPES was stained red, because it trapped the ethidium bromide fluorescent probe (Rounds et al., 2011); Viability of C8-D1A (D), HMC3 (E), SH-SY5Y (F), and HOG (G) cells printed in $P_{3.8}Ca_{20}Coll$ -DMEM HEPES inks and cultured over time. Results from the resazurin-based assay. Mean \pm SD, at least 4 replicates/condition. Data was analyzed with one-way ANOVA followed by Tukey's multiple comparisons test. ****: p -value < 0.0001 ; ***: p -value < 0.001 ; **: p -value < 0.01 ; and *: p -value < 0.05 .

showed that collagen fibers enriching pectin matrix in $P_{3.8}Ca_{20}Coll$ -DMEM HEPES were crosslinked together forming a dense network. The immunogold assay (Figure 8C") confirmed the specific localization of the gold-conjugated secondary antibody associated with collagen fibers at both 60 min and 4 h (arrow in C"). In contrast, a loose and uniform-looking matrix was observed in $P_{3.8}Ca_{20}$ -DMEM, in which collagen fibers were absent (Figures 8E,E'). In $P_{3.8}Ca_{20}Coll$ -DMEM HEPES embedding C8-D1A astrocytic-like cells (Figure 8F), the matrix surrounding the cells appeared more compact and denser (Figures 8F-H).

3.5 Direct cytocompatibility after 3D-bioprinting

A necessary condition to support cell proliferation in $P_{3.8}Ca_{20}Coll$ -DMEM HEPES is that cells survive the embedding process and the extrusion-based 3D-bioprinting with different cell types (SH-SY5Y human neuroblastoma cells, C8-D1A mouse astrocytes, HMC3 human microglial cells, and HOG human oligodendrogloma cells). For this reason, we evaluated cell viability immediately ($t \leq 60$ min) after bioprinting. Cell

viability (i.e. the number of live cells with respect to the total number of counted cells, Figure 9A) was similar for HOG cells, SH-SY5Y cells, C8-D1A cells, and slightly lower for HMC3 cells ($(73 \pm 10) \%$ vs. $\sim 90\%$). Cell counts were carried out after dissolving the constructs with sodium citrate, a Ca^{2+} chelating agent with improved cytocompatibility with respect to ethylenediaminetetraacetic acid (EDTA, Amaral et al., 2007). To speed up the disaggregation process, we coupled chemical and mechanical actions by pipetting sodium citrate on the constructs for a few minutes. As the process required manipulations after embedding and 3D-bioprinting, our results underestimated cell viability. The fact that cell viability was always comparable with controls supports the potential of $\text{P}_{3.8}\text{Ca}_{20}\text{Coll-DMEM HEPES}$ for the 3D-bioprinting of neural cells.

Although derived from pectin solutions in the same pH range, cell constructs were printed at different pressures (Figure 9A), sometimes greater than those for cell-free samples. We observed that the presence of cells could influence the viscoelastic properties (data not shown). For instance, hydrogels with SH-SY5Y and HMC3 cells shared comparable crosslinking kinetics, with minimal changes of viscoelastic properties over time with respect to their cell-free counterparts. After 40 min crosslinking, for samples with SH-SY5Y cells, G' and G'' reduced by 5% and 3%, while for samples with HMC3 cells, G' and G'' decreased by 7% and 2%. On the contrary, C8-D1A cells acted as a reinforcement for $\text{P}_{3.8}\text{Ca}_{20}\text{Coll-DMEM HEPES}$. G' and G'' increased by 51%, and 41% with respect to cell-free samples, respectively (data not shown).

Cell-laden $\text{P}_{3.8}\text{Ca}_{20}\text{Coll-DMEM HEPES}$ maintained the shear-thinning behavior, but we observed an increase in viscosity values over crosslinking time. The presence of cells reduced the ability of the material to be extruded through the nozzle, and required an increase in printing pressure. In addition, cells were embedded at high densities. To obtain a homogeneous cell dispersion and avoid aggregation, frequent mixing phases were required, leading to the formation of air bubbles. We speculate that it could explain the high pressures required for HOG-laden constructs. Indeed, visual inspections suggested that HOG cells were the biggest used in this study and thus potentially subjected to a fast sedimentation within the polymer solutions.

Since multiple grids can be printed from the same cartridge, we exploited the results in Figure 9A to investigate whether the increasing pressure could compromise cell survival (Figure 9B). For all the cell populations, the first set of scaffolds showed the highest viability, but a reduction was observed with increasing pressure (i.e. over time). For instance, about 100% of SH-SY5Y cells in the first three constructs (printed at 23 kPa) were viable, but viability dropped to 84% when pressure was increased to 60 kPa. On the contrary, the viability of HMC3 cells showed a drastic decrease after the second set of grids (from 81% at 28 kPa to 58% at 56 kPa).

Sample observation by confocal microscopy (Figure 9C) highlighted that the printing protocol did not affect cell viability, also showing that cells were homogeneously distributed within the inks. In fact, they were visible in the

green channel, meaning that they internalized the calcein-AM probe. The red background could be explained by ethidium homodimer-1 (sharing structural similarities with propidium iodide), which competed with Ca^{2+} in labelling pectin, as results from the literature (Rounds et al., 2011).

To strengthen the results from the trypan blue exclusion assay, viability after 3D-bioprinting was evaluated for all cell populations by a resazurin-based assay after 1 h, 1, 3 (or 4), and eventually 7 days of culture (Figures 9D–G). For all cell populations, viability increased over time. After embedding and 3D-bioprinting in $\text{P}_{3.8}\text{Ca}_{20}\text{Coll-DMEM HEPES}$, cells survived and kept their proliferative potential, suggesting that the proposed ink could be suitable to print and culture neural cells.

4 Discussion

Pectin and calcium concentrations tested in this study allowed to obtain 3D hydrogels mimicking the basic viscoelastic properties of brain tissue. In fact, at the end of time sweep scans, the elastic moduli of both gels in 0.9% w/v NaCl and DMEM w/and w/o HEPES fell in the range reported for brain tissue (i.e. from few hundreds of Pa to kPa, Leipzig and Shoichet, 2009; Axpe et al., 2020). $\text{P}_{2.4}\text{Ca}_{35}\text{-NaCl}$ showed the highest viscoelastic properties ($G' = 1.41 \times 10^3$ Pa; $G'' = 0.27 \times 10^3$ Pa), with $\tan\delta$ being about 0.2 (i.e. G'' being about 20% G'), as is often found in physiological tissues (Charrier et al., 2018). All the other hydrogels also fulfilled condition $0.1 < \tan\delta < 0.2$ (i.e. $10\% G' < G'' < 20\% G'$). Also due to its composition, we exploited $\text{P}_{3.8}\text{Ca}_{20}\text{Coll-DMEM HEPES}$ for the 3D-bioprinting of neural cells and showed that internally crosslinked pectin-based hydrogels could be suitable for neural cell culture.

This work demonstrates that pectin-based inks produced by pre-crosslinking by internal gelation allow to fabricate self-standing fibers and multi-layer grids with a defined shape after extrusion. Additives or post-printing treatments were shown to be not required. Ink development was guided by the effects of pH and pectin concentration on the viscosity of solutions, together with the impact of the amount of the crosslinker, i.e. the content of calcium salts, on the viscoelastic properties and printability of the gels. Since solvent composition is fundamental to develop a printable ink, we decided to increase complexity to catch up common basic elements and speed up the optimization. Firstly, we tested pectin solutions in 0.9% w/v NaCl, then solutions in DMEM with additives and finally in DMEM also supplemented with HEPES. Our method exploited rheology to give *a priori* information about ink printability and it coupled pH and printing time to gain full control over the kinetics of internal crosslinking. By introducing the pH of pectin solutions as a further parameter to be controlled, we were able to have multiple (pH-dependent) crosslinking kinetics without varying hydrogel composition. Basically, we added a tuning parameter to the time and expanded the

potential of the previously described 3D-reactive printing strategy (Sardelli et al., 2021). This opens to the possibility of applying this approach also to materials whose crosslinking kinetics depended on the pH. Overall, whatever the parameter that controls the crosslinking kinetics, it is possible to exploit it to modulate the printing time, i.e. the stage of the crosslinking in which a hydrogel in formation can be printed. In our case, this was strategic to minimize the persistence time of the cells in the ink before printing, while still allowing for a proper viscosity control.

The content of the crosslinking agent, i.e. CaCO_3 as a source of Ca^{2+} , was also a key parameter to determine the presence of insoluble deposits, fiber quality, and printing time. Pectin solutions at a concentration of 2.4% w/v in 0.9% w/v NaCl showed an acidic pH (3.4 ± 0.1), which was able to trigger a fast gelation even when mixed to the lower CaCO_3 concentration (20 mM). This concentration also allowed to avoid calcium deposits in printed fibers. In contrast, the higher concentration (35 mM CaCO_3) resulted in high pressures for extrusion-based 3D-printing (Figure 4). An increase in CaCO_3 , that correlates with enhanced hydrogel stiffness and reduced diffusion, may decrease cell viability and proliferation (Banerjee et al., 2009; Ahn et al., 2012). Thus, we produced internal crosslinking with 20 mM CaCO_3 .

Keeping in mind both 3D-printing and cellular studies, we controlled ink compositions to tune their properties. More specifically, starting from the hypothesis that solutions with comparable viscosity profiles exhibit similar printability in the presence of the same amount of CaCO_3 , we identified a suitable pectin concentration to reproduce the flow curve for the printable 2.4% w/v pectin in 0.9% w/v NaCl including a cell culture medium (DMEM). Moreover, to mimic common cell culture conditions, we enriched basal DMEM with serum, L-glutamine and antibiotics. The buffering capacity of DMEM was required to increase pectin concentration to 4% w/v to meet similar values of viscosity. The change from 0.9% w/v NaCl to DMEM speeded up the crosslinking kinetics in the early phase (20 min) and increased G'' (Figures 2C, D). In the recovery curves at 0 min (Supplementary Figures S1A, B), G'' values were greater for the ink produced in DMEM than in NaCl, but after 30 and 60 min crosslinking, the recovery trends of G'' were similar. The shift to DMEM also impacted extrudability (Supplementary Figures S1C–E) at time 0, when $\text{P}_{2,4}\text{Ca}_{20}$ -NaCl could be extruded more easily than P_4Ca_{20} -DMEM. At 30 and 60 min, extrudability depended on the shear rate: for shear rates lower than 10 s^{-1} , the extrusion of DMEM ink was easier than the one of the NaCl ink; for higher shear rates, the opposite occurred. The comparison between the printability windows of $\text{P}_{2,4}\text{Ca}_{20}$ -NaCl and P_4Ca_{20} -DMEM highlighted the effect of G'' : after 30 and 60 min, the maximum pressures to extrude P_4Ca_{20} -DMEM were like the ones for $\text{P}_{2,4}\text{Ca}_{35}$ -NaCl, but at 0 min they were even greater, and thus excessive for extrusion-based 3D-bioprinting.

To reduce hydrogel G'' without remarkable impact on the crosslinking kinetics, we decreased pectin concentration to 3.8%

w/v without varying pH (3.5 ± 0.1) and produced $\text{P}_{3,8}\text{Ca}_{20}$ -DMEM. The shift also reduced the maximum pressures for extrusion to values like the ones for $\text{P}_{2,4}\text{Ca}_{20}$ -NaCl.

But still, we needed to optimize the produced bioink for cell cultures by acting on the pH in the early stages of crosslinking. Towards this aim, the CO_2 /bicarbonate system already in basal DMEM (44 mM NaHCO_3) was coupled with HEPES. This supplementation did not vary the viscosity of the solution (Supplementary Figure S1F). To improve the cell adhesion properties of pectin (Chen et al., 2018) with a strategy simpler and cheaper than grafting with motif peptides, cells were loaded into collagen solutions at neutral pH and then mixed to pectin/ CaCO_3 3 min after the beginning of crosslinking. With this protocol, cells were loaded into pectin gels with pH around 5.81. Cell culture medium was immediately added to speed up the reaching of physiological pHs. For this reason, $\text{P}_{3,8}\text{Ca}_{20}\text{Coll}$ -DMEM HEPES was selected for 3D-bioprinting. For its preparation, solutions with $3.55 < \text{pH} < 3.70$ were used. However, even small pH variations have a remarkable effect on the viscoelastic properties of the final gels (Supplementary Figure S1G). When pH increased from 3.55 to 3.75, G' and G'' decrease. After 60 min crosslinking, for solutions with $3.55 < \text{pH} < 3.60$, G' and G'' reached 661 Pa and 73 Pa, respectively. For solutions with $3.71 < \text{pH} < 3.75$, G' and G'' reduced to 213 Pa and 43 Pa, respectively. For $\text{pH} > 3.79$, gelation did not occur in 1 h. The pH of pectin solutions was always measured prior the experiments because it was shown to also influence the crosslinking kinetics and the resting time (i.e. the time before printing constructs with uniform fibers and open porosities): the higher the pH was, the slower was the crosslinking kinetics and the longer the resting time before printing self-standing fibers. This needed to be considered to optimize the viscosity, the printing velocity, and the printing pressure.

Finally, our study proposes an innovative way of exploiting pectin/collagen combinations. Interactions based on surface patch binding were described in collagen/pectin composites loaded with bioactive glass nanoparticles (Wenpo et al., 2015; Goel et al., 2021). As results from previous works, pectin and collagen exhibit the same net charge, but the positively charged patches on collagen bind to the negatively charged segments on pectin, and Ca^{2+} acts as a bridge between —C=O and —COO groups (Goel et al., 2021). When neutral pectin/collagen solutions are combined (Jayakumar et al., 2014), the basic amino acids of collagen primarily interact with pectin, that stabilizes collagen by hydrogen bonding. It creates an effective defense mechanism against collagenase, and promotes collagen stability. Interestingly, an increase in pectin concentration (i.e. in the number of interaction sites) limits the mobility of collagen molecules, leading to the formation of collagen fibrils in the ordered form of precipitates. The mixing in neutral conditions of alkaline de-esterified pectin/ CaCl_2 with different ratios of collagen type I and/or IV (and the subsequent incubation at 37°C) was reported to create an optimal microenvironment for glioblastoma treatment (Belousov et al., 2020).

With these results in mind, together with the possibility of using our inks both for the realization of *in vitro* 3D models of neural tissue, and for cell delivery in clinical practice (e.g. stroke), we deeply focused on ink development and cell encapsulation. The exploitation of pectin as the bulk material provides an extremely varied skeleton on which it is potentially possible to graft molecules and signals to modulate cell behavior. The change from external to internal crosslinking allowed to achieve homogeneous hydrogels, with advantages in terms of providing uniform stimuli for cell culture. By mixing neutral collagen with a high pectin concentration, we speeded up collagen aggregation, and removed the need for incubation at 37°C. The proposed ink was suitable to produce multiple stacks of grids by 3D-printing, and promoted the adhesion of cells to the matrix, favoring their viability over time. Not only cells survived and proliferated after 3D-bioprinting, but they also interacted with the ink, as suggested by the time sweeps of cell-laden constructs. In addition, the structural reorganization of the hydrogels observed by TEM was probably cell-mediated and achieved thanks to the interaction between the matrix and the cell membranes (Figures 8F–H), leading to a change in the orientation of collagen fibers (Webber et al., 2016; Lovrak et al., 2017). Finally, with respect to clinical applications, a strict control over the pH of pectin solution allowed to tune the crosslinking kinetics, i.e. the time available to the ink to conform to the defect to be filled.

Data availability statement

The original contributions presented in the study are included in the article/Supplementary Material, further inquiries can be directed to the corresponding author.

Author contributions

MM, Software, Investigation, Visualization, Data Curation, Writing; LS, Rheological analyses: Methodology, Review and Editing; NB, Transmission electron microscopy: Investigation and Visualization; AG, Transmission electron microscopy: Methodology, Resources and Data Curation, Review and Editing; EJ, Confocal microscopy: Investigation, Visualization and Data Curation; MTR, Resources; FB-V, Rheological

References

- Ahn, S., Lee, H., Bonassar, L. J., and Kim, G. H. (2012). Cells (MC3T3-E1)-laden alginate scaffolds fabricated by a modified solid-freeform fabrication process supplemented with an aerosol spraying. *Biomacromolecules* 13, 2997–3003. doi:10.1021/bm3011352
- Amaral, K. F., Rogero, M. M., Fock, R. A., Borelli, P., and Gavini, G. (2007). Cytotoxicity analysis of EDTA and citric acid applied on murine resident

analyses: Methodology and Resources, Supervision, Review and Editing; PP, Conceptualization, Resources, Supervision, Writing, Review and Editing; MT, Conceptualization, Supervision, Project administration, Funding acquisition, Writing, Coordination of Review and Editing.

Acknowledgments

We thank Herbstreith and Fox for kindly gifting pectin. We are also very grateful to Sara Mantero (Politecnico di Milano) for the constructive support and useful discussions and to Diego Albani (Istituto di Ricerche Farmacologiche Mario Negri IRCCS) for kindly providing HMC3 cells. A special thanks to Francesca Annis, Maria Carolina Quintero Carmona, and Gloria Romero Vega (Politecnico di Milano) for technical support and to Alice Meroni and the Research Office (Politecnico di Milano) for administrative support. We also thank Luciana Borrelli for her final linguistic revision of the manuscript.

Conflict of interest

The authors declare that the research was conducted in the absence of any commercial or financial relationships that could be construed as a potential conflict of interest.

Publisher's note

All claims expressed in this article are solely those of the authors and do not necessarily represent those of their affiliated organizations, or those of the publisher, the editors and the reviewers. Any product that may be evaluated in this article, or claim that may be made by its manufacturer, is not guaranteed or endorsed by the publisher.

Supplementary material

The Supplementary Material for this article can be found online at: <https://www.frontiersin.org/articles/10.3389/fbioe.2022.1032542/full#supplementary-material>

macrophages culture. *Int. Endod. J.* 40, 338–343. doi:10.1111/j.1365-2591.2007.01220.x

Andriotis, E. G., Eleftheriadis, G. K., Karavasili, C., and Fatouros, D. G. (2020). Development of bio-active patches based on Pectin for the treatment of Ulcers and wounds using 3D-bioprinting technology. *Pharmaceutics* 12, 56. doi:10.3390/pharmaceutics12010056

- Antill-O'Brien, N., Bourke, J., and O'Connell, C. D. (2019). Layer-by-layer: The case for 3D bioprinting neurons to create patient-specific epilepsy models. *Materials* 12, 3218. doi:10.3390/ma12193218
- Appe, E., Orive, G., Franze, K., and Appel, E. A. (2020). Towards brain-tissue-like biomaterials. *Nat. Commun.* 11, 3423. doi:10.1038/s41467-020-17245-x
- Bae, M., Hwang, D. W., Ko, M. K., Jin, Y., Shin, W. J., Park, W., et al. (2021). Neural stem cell delivery using brain-derived tissue-specific bioink for recovering from traumatic brain injury. *Biofabrication* 13, 044110. doi:10.1088/1758-5090/ac293f
- Banerjee, A., Arha, M., Choudhary, S., Ashton, R. S., Bhatia, S. R., Schaffer, D. V., et al. (2009). The influence of hydrogel modulus on the proliferation and differentiation of encapsulated neural stem cells. *Biomaterials* 30, 4695–4699. doi:10.1016/j.biomaterials.2009.05.050
- Bedini, E., Iadonisi, A., Schiraldi, C., Colombo, L., Albani, D., Petrini, P., et al. (2021). Microbiological-chemical sourced chondroitin sulfates protect neuroblastoma SH-SY5Y cells against oxidative stress and are suitable for hydrogel-based controlled release. *Antioxidants* 10, 1816. doi:10.3390/antiox10111816
- Belousov, A., Titov, S., Shved, N., Malykin, G., Kovalev, V., Suprunova, I., et al. (2020). Hydrogels based on modified pectins capable of modulating neural cell behavior as prospective biomaterials in glioblastoma treatment. *Int. Rev. Neurobiol.* 151, 111–138. doi:10.1016/bs.im.2020.03.025
- Boulaoui, S., Al Hussein, G., Khan, K. A., Christoforou, N., and Stefanini, C. (2020). An overview of extrusion-based bioprinting with a focus on induced shear stress and its effect on cell viability. *Bioprinting* 20, e00093. doi:10.1016/j.bprint.2020.e00093
- Burey, P., Bhandari, B. R., Howes, T., and Gidley, M. J. (2008). Hydrocolloid gel particles: Formation, characterization, and application. *Crit. Rev. Food Sci. Nutr.* 48, 361–377. doi:10.1080/10408390701347801
- Campiglio, C. E., Carcano, A., and Draghi, L. (2021). RGD-pectin microfiber patches for guiding muscle tissue regeneration. *J. Biomed. Mater. Res. A* 110, 515–524. doi:10.1002/jbm.a.37301
- Causton, B. E. (1984). Improved bonding of composite restorative to dentine. A study *in vitro* of the use of a commercial halogenated phosphate ester. *Br. Dent. J.* 156, 93–95. doi:10.1038/sj.bdj.4805276
- Celus, M., Kyomugasho, C., Van Loey, M., Grauwet, T., and Hendrickx, M. E. (2018). Influence of pectin structural properties on interactions with divalent cations and its associated functionalities. *Compr. Rev. Food Sci. Food Saf.* 17, 1576–1594. doi:10.1111/1541-4337.12394
- Charrier, E. E., Pogoda, K., Wells, R. G., and Janmey, P. A. (2018). Control of cell morphology and differentiation by substrates with independently tunable elasticity and viscous dissipation. *Nat. Commun.* 9, 449. doi:10.1038/s41467-018-02906-9
- Chen, S., Cui, S., Zhang, H., Pei, X., Hu, J., Zhou, Y., et al. (2018). Cross-linked pectin nanofibers with enhanced cell adhesion. *Biomacromolecules* 19, 490–498. doi:10.1021/acs.biomac.7b01605
- Chesler, M. (2003). Regulation and modulation of pH in the brain. *Physiol. Rev.* 83, 1183–1221. doi:10.1152/physrev.00010.2003
- Cidonio, G., Glinka, M., Dawson, J. I., and Oreffo, R. O. C. (2019). The cell in the ink: Improving biofabrication by printing stem cells for skeletal regenerative medicine. *Biomaterials* 209, 10–24. doi:10.1016/j.biomaterials.2019.04.009
- Copus, P. W., Lee, S. J., and Atala, A. (2022). "Bioink printability and methodologies for cell-based extrusion bioprinting," in *3D bioprinting and nanotechnology in tissue engineering and regenerative medicine*. Editors L. J. Zhang, J. P. Fisher, and K. W. Leong. Second Edition (Elsevier Academic Press), 153–183.
- Danielyan, L., Schäfer, R., von Ameln-Mayerhofer, A., Buadze, M., Geisler, J., Klopfer, T., et al. (2009). Intranasal delivery of cells to the brain. *Eur. J. Cell Biol.* 88, 315–324. doi:10.1016/j.ejcb.2009.02.001
- Dennis, J. O., Adam, A. A., Ali, M. K. M., Soleimani, H., Bin Abd Shukur, M. F., Ibaouf, K. H., et al. (2022). Substantial proton ion conduction in methylcellulose/pectin/ammonium chloride based solid nanocomposite polymer electrolytes: Effect of ZnO nanofiller. *Membranes* 12, 706. doi:10.3390/membranes12070706
- Flinck, M., Kramer, S. H., and Pedersen, S. F. (2018). Roles of pH in control of cell proliferation. *Acta Physiol. (Oxf.)* 223, e13068. doi:10.1111/apha.13068
- Gao, X., Zhi, Y., Sun, L., Xue, H., Tai, G., Zhou, Y., et al. (2013). The inhibitory effects of a rhamnogalacturonan I (RG-I) domain from ginseng pectin on galectin-3 and its structure-activity relationship. *J. Biol. Chem.* 288, 33953–33965. doi:10.1074/jbc.M113.482315
- García-Revilla, J., Boza-Serrano, A., Espinosa-Oliva, A. M., Sarmiento Soto, M., Deierborg, T., Ruiz Rocio, R., et al. (2022). Galectin-3, a rising star in modulating microglia activation under conditions of neurodegeneration. *Cell Death Dis.* 13, 628. doi:10.1038/s41419-022-05058-3
- Giacoppo, S., Galuppo, M., Calabrò, R. S., D'Aleo, G., Marra, A., Sessa, E., et al. (2014). Heavy metals and neurodegenerative diseases: An observational study. *Biol. Trace Elem. Res.* 161, 151–160. doi:10.1007/s12011-014-0094-5
- Giampietro, R., Spinelli, F., Contino, M., and Colabufo, N. A. (2018). The pivotal role of copper in neurodegeneration: A new strategy for the therapy of neurodegenerative disorders. *Mol. Pharm.* 15, 808–820. doi:10.1021/acs.molpharmaceut.7b00841
- Gillispie, G., Prim, P., Copus, J., Fisher, J., Mikos, A. G., Yoo, J. J., et al. (2020). Assessment methodologies for extrusion-based bioink printability. *Biofabrication* 12, 022003. doi:10.1088/1758-5090/ab6f0d
- Goel, H., Gupta, N., Santhiya, D., Dey, N., Bohidar, H. B., and Bhattacharya, A. (2021). Bioactivity reinforced surface patch bound collagen-pectin hydrogel. *Int. J. Biol. Macromol.* 174, 240–253. doi:10.1016/j.ijbiomac.2021.01.166
- Hopkins, A. M., DeSimone, E., Chwalek, K., and Kaplan, D. L. (2015). 3D *in vitro* modeling of the central nervous system. *Prog. Neurobiol.* 125, 1–25. doi:10.1016/j.pneurobio.2014.11.003
- Jayakumar, G. C., Usharani, N., Kawakami, K., Rao, J. R., and Nair, B. U. (2014). Studies on the physico-chemical characteristics of collagen-pectin composites. *RSC Adv.* 4, 63840–63849. doi:10.1039/C4RA10368H
- Kar, F., and Arslan, N. (1999). Effect of temperature and concentration on viscosity of orange peel pectin solutions and intrinsic viscosity-molecular weight relationship. *Carbohydr. Polym.* 40, 277–284. doi:10.1016/S0144-8617(99)00062-4
- Kim, E., Seok, J. M., Bin Bae, S., Park, S. A., and Park, W. H. (2021). Silk fibroin enhances cytocompatibility and dimensional stability of alginate hydrogels for light-based three-dimensional bioprinting. *Biomacromolecules* 22, 1921–1931. doi:10.1021/acs.biomac.1c00034
- Kumar, M., Tomar, M., Saurabh, V., Mahajan, S., Punia, S., del Mar Contreras, M., et al. (2020). Emerging trends in pectin extraction and its anti-microbial functionalization using natural bioactives for application in food packaging. *Trends Food Sci. Technol.* 105, 223–237. doi:10.1016/j.tifs.2020.09.009
- Lara-Espinoza, C., Carvajal-Millán, E., Balandrán-Quintana, R., López-Franco, Y., and Rascón-Chu, A. (2018). Pectin and pectin-based composite materials: Beyond food texture. *Molecules* 23, 942. doi:10.3390/molecules23040942
- Lee, H., McKeon, R. J., and Bellamkonda, R. V. (2010). Sustained delivery of thermostabilized chABC enhances axonal sprouting and functional recovery after spinal cord injury. *Proc. Natl. Acad. Sci. U. S. A.* 107, 3340–3345. doi:10.1073/pnas.0905437106
- Leipzig, N. D., and Shoichet, M. S. (2009). The effect of substrate stiffness on adult neural stem cell behavior. *Biomaterials* 30, 6867–6878. doi:10.1016/j.biomaterials.2009.09.002
- Lessa, E. F., Medina, A. L., Ribeiro, A. S., and Fajardo, A. R. (2020). Removal of multi-metals from water using reusable pectin/cellulose microfibers composite beads. *Arab. J. Chem.* 13, 709–720. doi:10.1016/j.arabcj.2017.07.011
- Li, H., Li, N., Zhang, H., Zhang, Y., Suo, H., Wang, L., et al. (2020). Three-dimensional bioprinting of perfusable hierarchical microchannels with alginate and silk fibroin double cross-linked network. *3D Print. Addit. Manuf.* 7, 78–84. doi:10.1089/3dp.2019.0115
- Liang, L., and Luo, Y. (2020). Casein and pectin: Structures, interactions, and applications. *Trends Food Sci. Technol.* 97, 391–403. doi:10.1016/j.tifs.2020.01.027
- Lindsay, C. D., Roth, J. G., LeSavage, B. L., and Heilshorn, S. C. (2019). Bioprinting of stem cell expansion lattices. *Acta Biomater.* 95, 225–235. doi:10.1016/j.actbio.2019.05.014
- Liu, Z., Bhandari, B., Prakash, S., Mantihal, S., and Zhang, M. (2019). Linking rheology and printability of a multicomponent gel system of carrageenan-xanthan-starch in extrusion based additive manufacturing. *Food Hydrocoll.* 87, 413–424. doi:10.1016/j.foodhyd.2018.08.026
- Lopez Hernandez, H., Souza, J. W., and Appel, E. A. (2021). A quantitative description for designing the extrudability of shear-thinning physical hydrogels. *Macromol. Biosci.* 21, e2000295. doi:10.1002/mabi.202000295
- Lovrak, M., Hendriksen, W. E. J., Maity, C., Mytnyk, S., van Steijn, V., Eelkema, R., et al. (2017). Free-standing supramolecular hydrogel objects by reaction-diffusion. *Nat. Commun.* 8, 15317. doi:10.1038/ncomms15317
- Lozano, R., Stevens, L., Thompson, B. C., Gilmore, K. J., Gorkin, R., Stewart, E. M., et al. (2015). 3D printing of layered brain-like structures using peptide modified gellan gum substrates. *Biomaterials* 67, 264–273. doi:10.1016/j.biomaterials.2015.07.022
- Mehrotra, S., Moses, J. C., Bandyopadhyay, A., and Mandal, B. B. (2019). 3D printing/bioprinting based tailoring of *in vitro* tissue models: Recent

- advances and challenges. *ACS Appl. Bio Mater.* 2, 1385–1405. doi:10.1021/acscabm.9b00073
- Moreira, H. R., Munarin, F., Gentilini, R., Visai, L., Granja, P. L., Tanzi, M. C., et al. (2014). Injectable pectin hydrogels produced by internal gelation: pH dependence of gelling and rheological properties. *Carbohydr. Polym.* 103, 339–347. doi:10.1016/j.carbpol.2013.12.057
- Munarin, F., Guerreiro, S. G., Grellier, M. A., Tanzi, M. C., Barbosa, M. A., Petrini, P., et al. (2011). Pectin-based injectable biomaterials for bone tissue engineering. *Biomacromolecules* 14, 568–577. doi:10.1021/bm101110x
- Munarin, F., Petrini, P., Barcellona, G., Roversi, T., Piazza, L., Visai, L., et al. (2014). Reactive hydroxyapatite fillers for pectin biocomposites. *Mater. Sci. Eng. C* 45, 154–161. doi:10.1016/j.msec.2014.09.003
- Oliveira, E. P., Malysz-Cymborska, I., Golubczyk, D., Kalkowski, L., Kwiatkowska, J., Reis, R. L., et al. (2019). Advances in bioinks and *in vivo* imaging of biomaterials for CNS applications. *Acta Biomater.* 95, 60–72. doi:10.1016/j.actbio.2019.05.006
- Papadimitriou, L., Manganas, P., Ranella, A., and Stratakis, E. (2020). Biofabrication for neural tissue engineering applications. *Mater. Today Bio* 6, 100043. doi:10.1016/j.mtbio.2020.100043
- Paxton, N., Smolan, W., Böck, T., Melchels, F., Groll, J., and Jungst, T. (2017). Proposal to assess printability of bioinks for extrusion-based bioprinting and evaluation of rheological properties governing bioprintability. *Biofabrication* 9, 044107. doi:10.1088/1758-5090/aa8dd8
- Peneda Pacheco, D., Suárez Vargas, N., Visentin, S., and Petrini, P. (2021). From tissue engineering to engineering tissues: The role and application of *in vitro* models. *Biomater. Sci.* 9, 70–83. doi:10.1039/D0BM01097A
- Pereira, R. F., Barrias, C. C., Bártolo, P. J., and Granja, P. L. (2018). Cell-instructive pectin hydrogels crosslinked via thiol-norbornene photo-click chemistry for skin tissue engineering. *Acta Biomater.* 66, 282–293. doi:10.1016/j.actbio.2017.11.016
- Qiu, B., Bessler, N., Figler, K., Buchholz, M.-B., Rios, A. C., Malda, J., et al. (2020). Bioprinting neural systems to model central nervous system diseases. *Adv. Funct. Mater.* 30, 1910250. doi:10.1002/adfm.201910250
- Rounds, C. M., Lubeck, E., Hepler, P. K., and Winship, L. J. (2011). Propidium iodide competes with Ca²⁺ to label pectin in pollen tubes and arabidopsis root hairs. *Plant Physiol.* 157, 175–187. doi:10.1104/pp.111.182196
- Samanipour, R., Tahmooreesi, H., Nejad, H. R., Hirano, M., Shin, S.-R., and Hoorfar, M. (2022). A review on 3D printing functional brain model. *Biomicrofluidics* 16, 011501. doi:10.1063/5.0074631
- Sardelli, L., Tunesi, M., Briatico-Vangosa, F., and Petrini, P. (2021). 3D-Reactive printing of engineered alginate inks. *Soft Matter* 17, 8105–8117. doi:10.1039/d1sm00604e
- Sarker, M. D., Naghieh, S., McInnes, A. D., Ning, L., Schreyer, D. J., and Chen, X. (2019). Bio-fabrication of peptide-modified alginate scaffolds: Printability, mechanical stability and neurite outgrowth assessments. *Bioprinting* 14, e00045. doi:10.1016/j.bprint.2019.e00045
- Secchi, E., Munarin, F., Alaimo, M. D., Bosisio, S., Buzzaccaro, S., Ciccarella, G., et al. (2014). External and internal gelation of pectin solutions: Microscopic dynamics versus macroscopic rheology. *J. Phys. Condens. Matter* 26, 464106. doi:10.1088/0953-8984/26/46/464106
- Skjåk-Bræk, G., Grasdalen, H., and Smidsrød, O. (1989). Inhomogeneous polysaccharide ionic gels. *Carbohydr. Polym.* 10, 31–54. doi:10.1016/0144-8617(89)90030-1
- Sriamornsak, P., Wattanakorn, N., and Takeuchi, H. (2010). Study on the mucoadhesion mechanism of pectin by atomic force microscopy and mucin-particle method. *Carbohydr. Polym.* 79, 54–59. doi:10.1016/j.carbpol.2009.07.018
- Taylor, S. J., Rosenzweig, E. S., McDonald, J. W., and Sakiyama-Elbert, S. E. (2006). Delivery of neurotrophin-3 from fibrin enhances neuronal fiber sprouting after spinal cord injury. *J. Control. Release* 113, 226–235. doi:10.1016/j.jconrel.2006.05.005
- Taylor, A. C. (1962). Responses of cells to pH changes in the medium. *J. Cell Biol.* 15, 201–209. doi:10.1083/jcb.15.2.201
- Tunesi, M., Raimondi, I., Russo, T., Colombo, L., Micotti, E., Brandi, E., et al. (2019). Hydrogel-based delivery of Tat-fused protein Hsp70 protects dopaminergic cells *in vitro* and in a mouse model of Parkinson's disease. *NPG Asia Mater.* 11, 28. doi:10.1038/s41427-019-0128-8
- Vancauwenbergh, V., Delele, M. A., Vanbiervliet, J., Aregawi, W., Verboven, P., Lammertyn, J., et al. (2018). Model-based design and validation of food texture of 3D printed pectin-based food simulants. *J. Food Eng.* 231, 72–82. doi:10.1016/j.jfoodeng.2018.03.010
- Vaz, V. M., and Kumar, L. (2021). 3D printing as a promising tool in personalized medicine. *AAPS PharmSciTech* 22, 49. doi:10.1208/s12249-020-01905-8
- Wan-Ping, V., Ravindra, P., Tey, B.-T., and Chan, E.-S. (2011). Comparison of alginate and pectin based beads for production of poultry probiotic cells. *J. Biosci. Bioeng.* 111, 294–299. doi:10.1016/j.jbiosc.2010.11.010
- Webber, M. J., Appel, E. A., Meijer, E. W., and Langer, R. (2016). Supramolecular biomaterials. *Nat. Mater.* 15, 13–26. doi:10.1038/nmat4474
- Wenpo, F., Gaofeng, L., Shuying, F., Yuanming, Q., and Keyong, T. (2015). Preparation and characterization of collagen-hydroxyapatite/pectin composite. *Int. J. Biol. Macromol.* 74, 218–223. doi:10.1016/j.ijbiomac.2014.11.031
- Zhang, X., Chen, X., Hong, H., Hu, R., Liu, J., and Liu, C. (2021). Decellularized extracellular matrix scaffolds: Recent trends and emerging strategies in tissue engineering. *Bioact. Mater.* 10, 15–31. doi:10.1016/j.bioactmat.2021.09.014
- Zhao, Z., Vizetto-Duarte, C., Moay, Z. K., Setyawati, M. I., Rakshit, M., Kathawala, M. H., et al. (2020). Composite hydrogels in three-dimensional *in vitro* models. *Front. Bioeng. Biotechnol.* 8, 611. doi:10.3389/fbioe.2020.00611
- Zhong, Y., and Bellamkonda, R. V. (2008). Biomaterials for the central nervous system. *J. R. Soc. Interface* 6, 957–975. doi:10.1098/rsif.2008.0071